NASA TECHNICAL NOTE

NASA TN D-6060

NASA TN D-6060

INVESTIGATION OF ENGINE-EXHAUST-AIRFRAME INTERFERENCE ON A CRUISE VEHICLE AT MACH 6

by James M. Cubbage and Frank S. Kirkham

Langley Research Center
Hampton, Va. 23365

NATIONAL AERONAUTICS AND SPACE ADMINISTRATION • WASHINGTON, D. C. • JANUARY 1971

1. Report No.	2. Government Accession No.	3. Recipient's Catalog No.
NASA TN D-6060		

4. Title and Subtitle	5. Report Date
INVESTIGATION OF ENGINE-EXHAUST-AIRFRAME INTERFERENCE ON A CRUISE VEHICLE AT MACH 6	January 1971
	6. Performing Organization Code
7. Author(s)	8. Performing Organization Report No.
James M. Cubbage and Frank S. Kirkham	L-6488
	10. Work Unit No.
9. Performing Organization Name and Address	722-01-10-10
NASA Langley Research Center Hampton, Va. 23365	11. Contract or Grant No.
	13. Type of Report and Period Covered
12. Sponsoring Agency Name and Address	Technical Note
National Aeronautics and Space Administration Washington, D.C. 20546	14. Sponsoring Agency Code

15. Supplementary Notes

16. Abstract

Results from an investigation of the effects of underexpanded engine exhaust flow on the aerodynamic performance and stability of a cruise airplane at Mach 6 are presented. The influence of wing reflex angle and nozzle geometry on exhaust flow interference effects was investigated on a flat-plate model. The experiments were conducted at a free-stream Reynolds number of 17.05×10^6 based on the length of the airplane model over a model angle-of-attack range of 0^o to 10^o and at nozzle static-pressure ratios from 1 to approximately 4.

17. Key Words (Suggested by Author(s))	18. Distribution Statement
Engine-airframe integration Jet interference Mach 6 vehicle	Unclassified – Unlimited

19. Security Classif. (of this report)	20. Security Classif. (of this page)	21. No. of Pages	22. Price*
Unclassified	Unclassified	63	$3.00

*For sale by the National Technical Information Service, Springfield, Virginia 22151

INVESTIGATION OF ENGINE-EXHAUST-AIRFRAME INTERFERENCE ON A CRUISE VEHICLE AT MACH 6

By James M. Cubbage and Frank S. Kirkham
Langley Research Center

SUMMARY

Lift, drag, and pitching-moment increments resulting from interference between the underexpanded exhaust flow from an airbreathing propulsion system and the wing undersurface of a cruise airplane and a flat plate have been determined experimentally at Mach 6 and compared with results from a simplified analysis of the flow. The flat-plate model was used primarily to determine the influence of nozzle geometry and wing reflex angle on interference effects. The airplane model was a blended wing-body configuration. The models were tested over an angle-of-attack range of 0^{o} to 10^{o}, and the nozzle static-pressure ratio of the simulated turboramjet propulsion system was varied from 1 to approximately 4. The test Reynolds number was 17.05×10^{6} based on the airplane model length.

The results show that incremental normal forces generated by the nozzle flow expanding along the undersurface of the models were adequately predicted by analysis of a flow model that accounted for primary momentum changes of the two-dimensional and axisymmetric nozzle flows. Operation of the axisymmetric nozzles at static-pressure ratios greater than about 1.3 increased the airplane model lift-drag ratio and simultaneously counterbalanced the pitching moment caused by the net thrust vector for flight conditions typical of Mach 6 cruise. An analysis of the effect of thrust vectoring and the effect of jet interference on the cruise range of a typical Mach 6 cruise airplane showed that interference generated by the flow from two-dimensional nozzles is about twice as effective as thrust vectoring in increasing cruise range, whereas three-dimensional effects reduced the interference benefits from axisymmetric nozzle flow to the effectiveness achieved by thrust vectoring.

INTRODUCTION

Efficient integration of the airframe and propulsion system to obtain maximum overall airplane performance is one of the major tasks in the design of airbreathing hypersonic vehicles. (See, for example, ref. 1.) In the Mach 6 speed range, the propulsion system

(inlet, engine, and nozzle) is generally housed in a nacelle-type installation, and factors such as engine location, installation drag, and engine exhaust flow impingement on adjacent surfaces have an important effect on airplane design and performance. This report is concerned with the airframe—propulsion-system integration problem at Mach 6 and, in particular, with the effect of underexpanded engine exhaust flow on airplane aerodynamics.

Lift augmentation and pitching-moment increments due to the relatively high pressure ramjet exhaust flow acting on the wing undersurface of a Mach 6 cruise configuration were examined analytically in references 2 and 3 to obtain a first-order result. (The engine location on the blended wing-body configuration considered was about 6 nozzle exit diameters upstream of the wing trailing edge and exposed a considerable amount of wing area to the nozzle exhaust flow.) Although substantial aerodynamic benefits were indicated, it was pointed out in reference 2 that a more realistic assessment than that provided by the idealized analysis was needed to evaluate properly the jet interference effects on hypersonic-airplane performance and to compare the benefits of jet interference with engine installation concepts using vectored thrust. Accordingly, the investigation reported herein was undertaken to determine the effect of nozzle-exit static-pressure ratio, nozzle geometry, wing reflex angle, and angle of attack on the lift, drag, and pitching-moment coefficients with underexpanded engine exhaust flow washing large areas of the wing undersurface. Both a flat-plate model and a modified 1/109-scale model of an airplane designed for Mach 6 cruise operation were used in the experimental investigation. Only those results pertinent to an overall assessment of hypersonic jet interference effects are discussed in the main body of the paper. Detailed model descriptions, derivations of equations, and presentation of basic data are presented in the appendixes.

SYMBOLS

A area, meters^2

C_D drag coefficient, $\dfrac{D}{q_\infty A_{ref}}$

C_F thrust coefficient, $\dfrac{F}{q_\infty A_{ref}}$

C_L lift coefficient, $\dfrac{L}{q_\infty A_{ref}}$

C_N normal-force coefficient, $C_p \dfrac{A_N}{A_{ref}}$

C_m pitching-moment coefficient, $\dfrac{\text{Pitching moment}}{q_\infty A_{ref} l_{ref}}$

C_p	pressure coefficient, $\frac{p - p_\infty}{q_\infty}$
$\overline{C}_p$	average pressure coefficient in spanwise (y) direction
D	drag, newtons
d	diameter, meters
F	nozzle thrust, newtons
h	height, meters
L	lift, newtons
l	length, meters
M	Mach number
p	pressure, newtons per meter^2
q	dynamic pressure, newtons per meter^2
T	temperature, kelvins
w	width, meters
x	distance downstream from nozzle exit plane parallel with nozzle center line (see fig. 1(a)), meters
y	horizontal distance perpendicular to center line of inlet-nozzle section (see fig. 1(a)), meters
α	angle of attack; angle between model reference line or center line and free-stream velocity vector, degrees
γ	ratio of specific heats
ϵ	flat-plate reflex angle downstream of nozzle exit plane (see fig. 1(a)), degrees

Subscripts:

cp	center of pressure
e	exit
g	gross
i	inlet
j	with nozzle flow
N	projected in horizontal plane through model reference line
n	net
o	without inlet-nozzle section
ref	reference
∞	test section or "free-stream" conditions
1	underwing conditions at nozzle exit plane

The phrase "nozzle pressure ratio" or "pressure ratio" refers to the nozzle exit static-pressure ratio p_e/p_1 unless stated otherwise. The term "engine-off" refers to the models without the inlet-nozzle section installed.

EXPERIMENTAL MODELS AND TEST PARAMETERS

The flat-plate model (fig. 1) was used for investigation of wing reflex angle and nozzle geometry effects and provided a known flow field ahead of the simulated propulsion system. Experimental data were obtained for this model with both two-dimensional (2-D) and axisymmetric nozzles over an angle-of-attack range of 0^o to 10^o at wing reflex angles of 0^o, 2^o, 4^o, and 6^o. The airplane model (fig. 2) was a blended wing-body configuration (ref. 4) with the propulsion system located well upstream of the wing trailing edge. This model was tested at angles of attack of 0^o, 2^o, 5^o, and 7^o with axisymmetric $\gamma_e = 1.26$ gas-mixture nozzles only. The simulated propulsion system on both models included an inlet designed to capture the approaching airflow to minimize disturbances in the external

flow that would have existed if the inlet had been faired closed. The inlet flow for both models was discharged rearward from the lee (top) side of the models.

Further details of the models, test procedures, instrumentation, and data reduction procedures are discussed in appendix A.

RESULTS AND DISCUSSION

Turboramjet engines, consisting of turboaccelerators for Mach numbers up to 3 and subsonic burning ramjets for higher speeds, have been proposed as propulsion systems for Mach 6 airplanes. The analysis of reference 2 showed that at cruise the nozzle flow for these engines will be underexpanded with nacelle exit areas equal to maximum engine diameters because of a compromise between maximum propulsion efficiency and engine nacelle drag. Figure 3 shows nozzle pressure ratio as a function of nacelle expansion ratio for typical ramjet component efficiencies at angles of attack from 0° to 8°. Also shown are the nozzle pressure ratios at Mach 6 cruise for in-line and wrap-around turboramjet engines installed on the blended wing-body airplane as determined from trajectory analysis. Pressure ratios of 2.5 for the in-line and 1.8 for the wrap-around turboramjets are of primary interest in this investigation.

Flat-Plate-Model Results

Incremental normal force due to nozzle flow.- Incremental normal forces on the flat-plate model due to nozzle flow are presented as a fraction of the nozzle gross thrust coefficient in figure 4(a) for the 2-D air nozzles and in figure 4(b) for the axisymmetric air nozzles. At a given pressure ratio and angle of attack, the nozzle gross thrust coefficient was assumed the same for all nozzle configurations. (See appendix A for the equation used to calculate $C_{F,g}$.) The incremental normal forces presented act perpendicular to the movable portion or flap of the flat-plate model, and p_1 in the ratio p_e/p_1 is the pressure that existed on the model surface with the inlet-nozzle section removed and is representative of the local pressure to which the jet exhaust expands.

Incremental normal-force coefficients for the 2-D nozzle (fig. 4(a)) were larger than those for the axisymmetric nozzles (fig. 4(b)) over the pressure-ratio range and were as high as 21 percent of the gross thrust coefficient at nozzle pressure ratios of 2 and above. As the nozzle pressure ratio decreases below 2, the force-thrust ratio for both nozzle configurations decreases rapidly and is substantially negative (-14 percent of the gross thrust coefficient) at $p_e/p_1 = 1$ for the axisymmetric nozzles with $\epsilon = 0^{\circ}$ (fig. 4(b)). This result for the axisymmetric nozzle configuration indicates that a lift penalty would be incurred if full-expansion nozzles $(p_e/p_1 = 1)$ were used in the propulsion system. The negative incremental normal-force coefficient for this pressure ratio results from

the nozzle flow aspirating the volume enclosed by the nozzle plumes and the plate surface. (See appendix B for pressure distributions on the flap surface.)

The calculated variation of $\frac{C_{N,j} - C_{N,o}}{C_{F,g}}$ for $\alpha = 5^o$ is also shown in figure 4. The procedure used for calculating incremental normal-force coefficients (eq. (B2)) effectively accounts for exhaust flow momentum changes downstream of the 2-D nozzles, and the agreement between calculated and experimental values is good (fig. 4(a)). Incremental normal-force coefficients for the axisymmetric nozzles (fig. 4(b)) were calculated by modifying the calculation procedure to account for the radial expansion of the exhaust momentum of the axisymmetric nozzles and to account for the contact or "footprint" areas of the nozzle plumes on the flap surface. These modifications only approximately account for the differences between the two flow fields so that the prediction of results for the axisymmetric nozzles is not as good as that for the 2-D nozzles. However, a satisfactory estimate for preliminary design purposes can be obtained by this procedure.

Although the incremental normal force due to nozzle flow can be substantial for certain conditions, the direction of this force at positive angles of attack produces drag as well as lift. Therefore, the overall effect of the nozzle flow on lift-drag ratio can be much smaller than might be anticipated from the value of the normal-force increment. Bending or reflexing the portion of the surface downstream of the nozzle-exit plane away from the nozzle center line reduces the drag component of the normal-force vector with some sacrifice in the lift increment. Consequently, a wing or flap reflex angle was included as a geometric variable in this investigation to determine an optimum value.

Effect of wing reflex angle ϵ.- In order to show the effect of reflex angle on the flat-plate model, incremental lift and drag coefficients derived from the incremental normal forces have been used together with aerodynamic characteristics typical of a Mach 6 airplane at $\alpha = 5^o$ $\left(C_{L,o} = 0.0753 \text{ and } C_{D,o} = 0.01645 \text{ for } (L/D)_o = 4.58\right)$ to estimate the improvement in L/D produced by jet interference. In figure 5 the lift-drag ratio with nozzle flow $(L/D)_j$ normalized with respect to the lift-drag ratio without nozzle flow $(L/D)_o$ is shown as a function of reflex angle and nozzle pressure ratio. For both nozzle configurations, the optimum value of ϵ is 0^o except at the two highest pressure ratios $\left(p_e/p_1 = 3 \text{ and } 4\right)$. At a pressure ratio of 2 for the 2-D nozzle in figure 5(a), there is little difference in performance between $\epsilon = 0^o$ and 2^o. In figure 5(b) at $\epsilon = 0^o$ operation of the axisymmetric nozzles at $p_e/p_1 = 1$ again results in a performance loss. Prediction of the experimental results is generally good at $\epsilon = 0^o$ for both nozzle configurations, but, with the exception of the two highest pressure ratios, the amount by which the data are overpredicted increases as ϵ increases. The discrepancy between calculated and experimental results for $\epsilon > 0^o$ is partly due to the difference between experimental and calculated drag coefficients since $(L/D)_j/(L/D)_o$ is sensitive to small changes in C_D.

Effect of γ_e on incremental normal-force coefficient.- The results of the investigation of the effect of γ_e on jet interference effects were inconclusive due to instrumentation failures. The results, however, do indicate that incremental normal forces due to jet effects increase as γ_e decreases. A more complete discussion of these results is presented in appendix B.

Airplane-Model Results

Incremental lift, drag, and pitching-moment coefficients due to nozzle flow.- Incremental lift, drag, and pitching-moment coefficients are presented as a function of nozzle pressure ratio in figure 6 for the four angles of attack. Coefficients for $\alpha = 0^o$ and 2^o are presented although schlieren photographs of the flow about the airplane model showed that the inlet was spilling some flow at these two values of α. The effect of the partially unstarted inlet on the data is not known with certainty. However, data obtained on the flat-plate model indicated that $C_{N,j}$ with the inlet unstarted was slightly less than that with the inlet started (about 0.00074 based on the airplane reference area) and was essentially constant regardless of nozzle pressure ratio and model angle of attack.

The calculated incremental lift, drag, and pitching-moment coefficients for $\alpha = 5^o$ (shown by the dashed curves in fig. 6) again indicate that the calculation procedure is adequate for preliminary design purposes. The undersurface of the airplane model washed by the nozzle flow was assumed to be flat in the spanwise direction in the calculation procedure since the spanwise curvature of the inlet-nozzle section matched the body curvature and since the radius of this curvature was large relative to the nozzle exit diameter.

Effect of nozzle flow on lift-drag ratio.- The effect of nozzle pressure ratio on the untrimmed lift-drag ratio of the airplane model is shown in figure 7. The variation of L/D with and without nozzle flow with angle of attack is shown in figure 7(a), and the variation of the ratio of $(L/D)_{j,max}$ to $(L/D)_{0,max}$ with nozzle pressure ratio is shown in figure 7(b). Figure 7(a) shows that jet interference at $p_e/p_1 = 2$ and 3 increases L/D of the airplane model over the angle-of-attack range. The increment in L/D for $p_e/p_1 = 1$ is negative and this performance loss was noted earlier for the flat-plate model with axisymmetric nozzles. The improvement in maximum L/D because of jet interference effects (fig. 7(b)) ranges from about 2 to 5 percent for pressure ratios of interest for Mach 6 cruise airplanes. (See fig. 3.) The effects of structural and thermal protection system weights on airplane performance that may result from acoustical and thermal loads imposed on the airframe by the nozzle flow washing the wing undersurface have not been considered in this investigation. Therefore, in a detailed system analysis and mission analysis of a prototype configuration, the net improvement in aerodynamic performance obtainable from jet interference effects may be altered from that presented.

Effect of nozzle flow on pitching-moment coefficient.- Pitching-moment coefficients for the airplane model are shown as a function of nozzle pressure ratio in figure 8 for three conditions: (1) airplane alone, (2) airplane alone plus the calculated moment from the net thrust vector, and (3) airplane alone plus moment from the net thrust vector plus the experimental moments from jet interference effects. The net thrust vector was assumed to act parallel to the model reference line. Note that the coefficient for the airplane alone is shown in figure 8 as a horizontal line for reference purposes.

The point where the reference line is crossed by the total moment coefficient line gives the pressure ratio at which the moment from the net thrust vector is canceled by the moment from jet interference. This cancellation occurs at $p_e/p_1 \approx 2$ for $\alpha = 5^o$ and 7^o (figs. 8(c) and (d)), and at $p_e/p_1 = 1.5$ for $\alpha = 0^o$ and 2^o (figs. 8(a) and (b)). Thus, for the configuration investigated, jet interference with the wing undersurface simultaneously improved L/D and canceled the nose-up pitching moment resulting from the engine thrust vector.

Comparison of Jet Interference Effects and Thrust Vectoring on Airplane Performance

The use of thrust vectoring or deflection to improve cruise range has been shown (ref. 5, for example) to be particularly applicable to hypersonic airplanes because the gross thrust (the quantity vectored) of an airbreathing propulsion system is much larger than the net thrust of the system at hypersonic speeds. A comparison of the improvement in cruise range for airplanes using either jet interference or thrust vectoring has been made by using the equations derived in appendix C. The variation of engine and aerodynamic parameters used in this analysis is shown as a function of nacelle expansion ratio A_e/A_i in figure 9. (See also fig. 3 for p_e/p_1 variation with A_e/A_i.) These parameters are typical of a Mach 6, turboramjet-powered, hypersonic transport during the cruise phase of the flight at an angle of attack of 5^o. Jet interference and lift force were obtained from figure 4 for $\epsilon = 0^o$. The interference forces from the flat-plate tests were used so that the superiority of 2-D nozzles over axisymmetric nozzles (assuming equal nozzle efficiencies) could be clearly demonstrated.

The relative merits of thrust vectoring and using jet interference lift are shown in figure 10. The curve labeled "no jet interference or thrust vectoring" would be typical of a configuration with the nozzle exit coincident with the wing trailing edge (e.g., the distinct wing-body configuration of ref. 2). If the gross thrust is deflected downward (curve labeled "thrust vectoring"), the cruise range of the airplane can be increased about 2.5 percent. The results for configurations using jet interference to increase cruise range show that interference from axisymmetric nozzles is as effective as thrust

vectoring while jet interference from 2-D nozzles is almost twice as effective as thrust vectoring in increasing cruise range.

The effectiveness of using jet interference to increase cruise range can be explained by noting that the lift produced by jet interference results from the continued expansion of the jet exhaust along the wing undersurface. Thus, the wing undersurface acts as a nozzle, controlling the expanding exhaust flow and deflecting it downward, achieving the dual effect of effectively increasing the nacelle expansion ratio and vectoring the thrust with no decrease in L/D. Configurations using thrust vectoring, on the other hand, achieve highly expanded nozzle flow only if the nacelle expansion ratio is increased with a resultant decrease in L/D.

The preceding discussion has assumed that the entire engine inlet and exhaust system is external to the basic airplane contours. This approach was used because if the exhaust nozzle penetrates the airplane contour, a reduction in available volume would result. However, it is of interest to observe that if the additional nozzle exit area required for full expansion of the nozzle flow were obtained by allowing the nozzle to penetrate the airplane contour (partially submerged nozzle), then maximum engine performance can be obtained at maximum L/D. The Breguet factor (appendix C) for this situation with optimum thrust vectoring (indicated by an arrow in fig. 10) is only about 1 percent greater than that obtained for jet interference effects from a 2-D nozzle.

SUMMARY OF RESULTS

An investigation of the effects of underexpanded flow from two-dimensional and axisymmetric nozzles on the aerodynamics of a flat-plate model and a model of a cruise-type airplane at Mach 6 yielded the following results:

1. Incremental normal forces generated by nozzle flow expanding along the undersurface of the flat-plate model ranged from -14 to 21 percent of the gross nozzle thrust, depending primarily on nozzle type, nozzle pressure ratio, and reflex angle. Adequate prediction of the normal forces was obtained by using a relatively simple flow model that accounted for primary momentum changes of the nozzle flow.

2. A two-dimensional nozzle produces greater incremental normal forces and, therefore, a greater potential for improvement in airplane performance than axisymmetric nozzles.

3. When the lift and drag components of the incremental normal-force vector obtained for the flat-plate model were used to estimate the improvement in lift-drag ratio for a typical Mach 6 cruise airplane, reflexing the model surface away from the nozzle center line increased the airplane lift-drag ratio for nozzle pressure ratios of 3

and above with the optimum reflex angle tending to increase with increasing nozzle pressure ratio. Below nozzle pressure ratios of 3, the optimum reflex angle was essentially 0^{o}.

4. Operation of the axisymmetric nozzles at a static-pressure ratio of 1 (fully expanded nozzle flow) on both the flat-plate and airplane models resulted in negative values of incremental normal force and a reduction in overall airplane performance.

5. The effect of nozzle flow on the aerodynamics of the airplane model was to increase the lift-drag ratio and to simultaneously counterbalance the moment due to the net thrust vector for cruise flight conditions (angles of attack from 5^{o} to 7^{o} and nozzle pressure ratio of about 2.0).

6. An analysis of the effect of thrust vectoring and the effect of jet interference on the Breguet factor for a typical Mach 6 cruise airplane shows that interference generated by the flow from two-dimensional nozzles is about twice as effective as thrust vectoring in increasing cruise range, whereas three-dimensional effects reduced the interference benefits from axisymmetric nozzle flow to the effectiveness achieved by thrust vectoring.

Langley Research Center,
National Aeronautics and Space Administration,
Hampton, Va., September 22, 1970.

APPENDIX A

APPARATUS AND METHODS

Models

A flat-plate model and a modified scale model of an airplane designed for Mach 6 cruise were used in this investigation. The flat-plate model simplified model changes for investigation of wing reflex angle and nozzle geometry effects and also provided a uniform flow ahead of the instrumented portion of the model. An inlet designed for full capture of the flow approaching the inlet was provided on both models to simulate the actual operation of the engines and to eliminate flow disturbances that would have been produced had the inlet been faired closed. The inlet flow was discharged rearward from the lee side of the models.

Flat-plate model.- The flat-plate model (fig. 1) was made of stainless steel and consisted of two sections: a 25.4-cm-square front section that attached to the support strut and an instrumented rear section or flap 17.78 cm long by 25.4 cm wide. This flap was attached to the front section through two support arms that projected rearward from the front section. A series of tapered blocks were used between the support arms and the flap to adjust the reflex angle ϵ from 0° to 6° in 2° increments. The joint between the two plate sections was in the plane of the nozzle exits, and a silicone rubber gasket was used to prevent air leakage through this joint.

The inlet-nozzle section was offset from the model center line to position the instrumented area of the flap between the Mach lines originating from the upstream corners of the model. (The Mach lines for $\alpha = 0^{\circ}$ are indicated by the dashed lines in fig. 1(a).) The support strut attachment point was offset in the opposite direction to provide clearance for the four nozzle supply tubes.

Sectional views of the 2-D and axisymmetric nozzles are included in figure 1(a). Two sets of axisymmetric nozzles were tested on the flat-plate model; one designed for airflow ($\gamma = 1.4$) through the nozzles and the other designed for the sulfur hexafluoride-nitrogen (SF_6-N_2) gas-mixture ($\gamma_e = 1.26$) flow through the nozzles. The nozzle section was mounted on the model such that the nozzle wall was tangent with the plate surface at the nozzle exit. A cover plate that mounted flush with the plate surface was used to close the openings in the plate left by the inlet-nozzle section when engine-off tests were made on the model.

Sideplates, shown by dashed lines in figure 1(a), were used for two test runs to determine whether cross flow existed over the flap surface.

Airplane model.- The airplane model (fig. 2) was a modified 1/109-scale model of a blended wing-body configuration developed during studies of hypersonic cruise vehicles

(ref. 3). Modifications to the configuration consisted of removing the vertical tail and removing a portion of the body above the upper wing surface between the support strut fitting and the rear end of the model. These modifications permitted access for installation and removal of the inlet-nozzle section and for installation of pressure leads to the static-pressure orifices. The model was cast and sanded to a smooth finish.

The inlet-nozzle section for the airplane model was of the same design as that for the flat-plate model except that it was shaped to fit the 11.18-cm-radius curvature of the model undersurface. The airplane model was tested only with the axisymmetric $\gamma_e = 1.26$ nozzle. A cover plate over the inlet-nozzle section openings was also used on this model during engine-off tests.

Nozzles.- A method-of-characteristics computer program (constant γ) was used to obtain the coordinates of the 2-D and axisymmetric nozzles used in this investigation. These coordinates (fig. 1(a)) were not corrected for boundary-layer growth because of the small size of the nozzles. The exit diameter of the axisymmetric nozzles was 2.032 cm and the center-to-center spacing between nozzles on the flat-plate model was 2.286 cm. The height of the 2-D nozzle was selected so that, for a constant nozzle-section width, the exit area (12.97 cm^2) of the 2-D nozzle was the same as the exit area of four axisymmetric nozzles. The design Mach number of the $\gamma = 1.26$ axisymmetric nozzle ($M_e = 3.7$) was based on the maximum engine diameter and ramjet throat area of the wrap-around turboramjet engine used in blended wing-body configuration of reference 3. The design Mach number of the $\gamma_e = 1.4$ nozzles ($M_e = 3.5$) was then selected so that the exhaust flow momentum would be equal to that of the $\gamma_e = 1.26$ nozzle at each nozzle pressure ratio.

Tunnel

This investigation was conducted in the Langley 20-inch Mach 6 tunnel at a stagnation pressure of 25 atm (1 atm = 101.325 kN/m^2) and a stagnation temperature of 480 K; the corresponding Reynolds number was 20.9×10^6 per meter or 17.05×10^6 based on the length of the airplane model.

Instrumentation

Static-pressure-orifice locations on the flat-plate model and on the airplane model are shown in figures 1(a) and 2(a), respectively. All orifices, including those at the nozzle exits, had a diameter of 1.016 mm, and the 1.524-mm-diameter tubing leading from these orifices was increased to 2.286-mm tubing as close as possible to the orifice. The nozzle manifold (fig. 11) contained a total-pressure and total-temperature probe and tunnel instrumentation consisted of stagnation-pressure and temperature probes and a total-pressure probe mounted in the test section. All pressures were measured by electrical

pressure transducers and the typical distance between a model static-pressure orifice and its transducer was about 2.4 m. The output from the transducers was recorded on magnetic tape and later processed by an electronic computer.

Model Installation and Nozzle Flow Supply System

Installation of the flat-plate model in the tunnel and a schematic of the nozzle flow supply system are shown in figure 11. Installation of the airplane model was essentially identical to that shown for the flat-plate model.

Model installation.- The models were supported "upside-down" in the tunnel by a single strut that was, in turn, mounted on the angle-of-attack sector located in a housing below the tunnel floor. The angle of attack of the models was variable from 0° to 10°. A cylindrical manifold to which the four nozzle supply tubes were connected was attached to the lower portion of the support strut. A flexible hose connected the manifold to the piping of the nozzle flow supply system. Pressure leads from the models were routed down the rear of the support strut and brought outside the tunnel through an opening of the angle-of-attack mechanism housing.

Nozzle flow supply system.- The main components of the nozzle flow supply system shown schematically in figure 11 are the storage tanks, pressure regulator, heat exchanger, preheated piping, and the control valve. The storage tanks had a combined volume of 0.85 m^3 and were electrically heated to about 350 K to insure conversion of the liquid sulfur hexafluoride (SF_6) to a gas during charging of the tanks. (SF_6 ordinarily exists as a liquid in the cylinders in which it is commercially shipped.) A dome-loaded pressure regulator was located downstream of the storage tanks and was set for a regulated downstream pressure of 40 atmospheres. The storage tanks were normally charged to about 67 atmospheres. The heat exchanger utilized an electrically heated chlorinated polyphenyl liquid as the heat exchange medium and the liquid was kept in constant motion by a motor-operated agitator. The piping between the heat exchanger and the control valve was double-wall piping with the inner piping carrying the nozzle flow. Service air, also heated by the heat exchanger, passed through the annulus between the inner pipe and the outer insulated pipe wall. The pneumatically operated control valve was located just outside the tunnel and was controlled remotely from the tunnel operating room.

The composition of the sulfur hexafluoride-nitrogen mixture needed to achieve a value of 1.26 for γ_e was 75 percent SF_6 and 25 percent N_2 by weight at a temperature of 422 K. The molecular weight of SF_6 is 146.06, and it is a nontoxic, nonflammable, highly stable gas used primarily as a dielectric in electrical switchgear and electronic devices. Mass spectrometer analyses of gas samples taken before and after test runs showed that the maximum deviation from the design gas mixture was less than 3 percentage points in the direction of excess nitrogen. Although the nozzle flow supply system

was designed specifically for the use of the SF_6-N_2 mixture, it was also used for the tests involving air for the nozzle flow. For these tests, a high pressure (67 atmospheres) air line was connected into the system and the storage tanks were continuously charged from this line during a test run. The operating temperature of the heat exchanger was lowered for the air tests so that the manifold stagnation temperature was nominally about 340 K as compared with 422 K for the SF_6-N_2 mixture.

Data Reduction

Test-section static and dynamic pressures.- Test-section, or free-stream, static and dynamic pressures were calculated from the measured values of tunnel stagnation pressure and test-section pitot pressure. Although the differences between the values of p_∞ and q_∞ obtained for each data point and the average values obtained for a test run were generally small, the values for each data point were used in computing aerodynamic coefficients. This procedure was used to reduce cumulative errors in computing incremental effects due to the nozzle flow.

Nozzle static pressure ratio.- Nozzle exit static pressures p_e were obtained from measured nozzle manifold pressures $p_{t,m}$ (where subscript t indicates total) by using a calibration of the pitot pressure at the nozzle throat p_t^* (where $*$ indicates at the nozzle throat) as a function of $p_{t,m}$ and by using an overall average exit Mach number derived from pitot pressure surveys across the nozzle exits. These calibrations were obtained during static tests conducted separately from the tunnel tests. Conversion of the pitot pressure surveys across the exits of the nozzles for the SF_6-N_2 mixture to Mach number profiles was accomplished through use of real-gas normal-shock-loss tables compiled for the calculated value of γ_e. The value of 1.26 for γ_e was, in turn, established from real gas calculations starting with known conditions at the nozzle throat ($\gamma^* = 1.16$, $T_t^* = 422$ K, and 72.9 percent SF_6 and 27.1 percent nitrogen mixture composition, for example).

Underwing or ambient static pressures p_1 were obtained for both models from engine-off tests. An arithmetic average of all static pressures measured on the flap at $\epsilon = 0^o$ was used for p_1 on the flat-plate model for all values of ϵ, whereas a single pressure, indicative of the pressure at the nozzle exit plane, was used for p_1 on the airplane model.

Aerodynamic coefficients.- Standard force and pressure coefficients were computed from the data with all pressure coefficients referenced to free-stream static and dynamic pressures unless otherwise noted. Forces acting on the models were obtained by assigning incremental normal and axial areas to each pressure orifice and numerically integrating the incremental forces assuming pressure symmetry about the center lines of the models. The moment center for the flat-plate model was taken at the juncture of

the nozzle exit plane and the flap surface. The location of the airplane model center of gravity is shown in figure 2(a).

Thrust coefficient.- Gross thrust coefficients for the nozzles were computed from the data by use of the following equation:

$$C_{F,g} = \frac{p_e A_e \left[\gamma_e M_e^2 + \left(1 - \frac{p_1}{p_e} \right) \right]}{A_{ref} q_\infty}$$

APPENDIX B

PRESENTATION OF BASIC DATA

Flat-Plate Pressure-Coefficient Distributions

A typical sampling of pressure coefficients determined from measured pressures on the flap surface of the flat-plate model is presented in figures 12 to 16 as a function of the distance downstream from the nozzle exit plane for the flat-plate model. These pressure-coefficient distributions are for an angle of attack of 5° and are typical of those obtained for other values of α. For those figures showing distributions obtained with nozzle flow, a nozzle exit pressure coefficient $C_{p,e}$ based on the average calibrated static pressure at the nozzle exit is given for each nozzle pressure ratio.

Model without inlet-nozzle section.- The flat-plate model was tested without the inlet-nozzle section to establish reference values of the underwing pressure p_1 and reference, or "engine-off," forces on the model. Figure 12 shows engine-off pressure-coefficient distributions for the $\epsilon = 0^{\circ}$ configuration for the several rows of pressure orifices. The distributions are essentially flat and are representative of those obtained for other values of α. A longitudinal pressure gradient existed near the nozzle exit plane on the $\epsilon > 0^{\circ}$ configurations because of boundary-layer effects over the physically sharp juncture between the forepart of the model and the flap. This pressure gradient is evident in figure 13 where the average spanwise engine-off pressure coefficient is plotted for the four values of ϵ. Figure 13 also shows that adding sideplates to the model at $\epsilon = 0^{\circ}$ and 4° had no effect on $\overline{C}_{p,o}$. Therefore, all subsequent data on the flat-plate model were obtained without the sideplates installed.

Model with two-dimensional nozzle.- Pressure-coefficient distributions on the flap surface along the center line of the two-dimensional nozzle are shown in figure 14 for several nozzle pressure ratios and for all values of ϵ. The ratio x/h_e is used for the distance downstream of the nozzle exit in this figure. The $\overline{C}_{p,o}$ distributions of figure 13 are indicated in the figure and two calculated distributions are shown for a pressure ratio of 3. One calculated distribution was obtained from a Prandtl-Meyer expansion calculation using 1° increments for the expansion fan originating at the lower nozzle lip and at the upper nozzle lip for the $\epsilon > 0^{\circ}$ configurations and the other distribution by the simple procedure of using only one average expansion wave to represent an entire expansion fan. The angle through which the nozzle flow at the lower nozzle lip was expanded was established by adjusting the angle until the pressure and flow direction of the nozzle flow after expanding were equal to the pressure and flow direction of the external flow adjacent to the plume. This angle ranged from 0° for $p_e/p_1 = 1.0$ to about 6.8° for $p_e/p_1 = 4.0$ at $\alpha = 10^{\circ}$.

APPENDIX B

For a given value of ϵ in figure 14, the pressure-coefficient distributions for the various pressure ratios are generally similar in appearance. Good agreement between the calculated and experimental pressure coefficients was obtained along the nozzle center line where the lower lip expansion fan impinged on the model, but agreement elsewhere along this line was poor. The coefficients downstream of the impingement region were smaller than predicted and those upstream of this region were not constant and were generally higher than predicted. The variation in $C_{p,j}$ as well as the higher level upstream of the impingement region is attributed primarily to nonuniformities in the flow from the nozzle and in the static pressure laterally across the nozzle. The lower than calculated values of $C_{p,j}$ downstream of the impingement region are due, in part, to expansion waves originating at the nozzle sides and to overexpansion at the nozzle exit due to the base area at the nozzle exit.

Model with axisymmetric nozzles.- Pressure-coefficient distributions on the flap surface along the center line of the inlet-nozzle section (located between the two inner nozzles) and along the center line of one of the nozzles are shown in figure 15 for three nozzle pressure ratios and for the range of flap angles. A distinct difference between the distributions for the two spanwise locations will be noted for all values of ϵ. For the $y/d_e = 0$ location (inlet-nozzle section center line), $C_{p,j}$ increases over a distance of about 1 nozzle diameter downstream of the nozzle exit plane, whereas along a nozzle center line $\left(y/d_e = 1.69\right)$, $C_{p,j}$ decreases over a somewhat smaller distance. The increase in $C_{p,j}$ along the line between adjacent nozzles is due to the pressure rise across the shock waves generated along the line of contact between the nozzle plumes and the line of contact of the plume and the surface. As the nozzle pressure ratio increases, the strength of these impingement shocks increases (larger contact angle between the plumes) with a corresponding increase in the pressure rise on the flap surface. The pressure coefficient at $x/d_e = 0.125$ for this line of pressure orifices is lower than $C_{p,o}$ because of the aspiration action of the two adjacent nozzle flows.

The rapid decrease in pressure coefficient on the flap surface, along the nozzle center line, results from the flap surface effectively cutting across contours of constant Mach number within the expanding flow. (These contours radiate from the nozzle lip and tend to become parallel with the nozzle center line, as the contour Mach number increases, before bending back towards the nozzle center line.) Although the flap prevents the nozzle flow in close proximity to the line through the tangent point of the nozzle exit and flap surface from expanding, the pressure orifices along this line sense pressures that are influenced by the expanding nozzle flow in the unrestricted portion of the plume. After adjacent nozzle plumes impinge on each other, a large portion of the plume is restricted with the result that pressures sensed by the orifices along the tangent point line (nozzle center line) remain nearly constant or decrease slowly over a distance of about 2 nozzle diameters. The impingement area on the flap surface for expansion waves from the lower

half of the nozzle lip is highly curved so that the decrease in $C_{p,j}$ within the impingement region for the axisymmetric nozzles is less pronounced than for the 2-D nozzles for which the impingement area is essentially a straight band running spanwise across the model. At $\epsilon = 0^o$ and $\epsilon = 2^o$ (figs. 15(a) and (b)), the pressure coefficient for $p_e/p_1 \approx 1.0$ is generally less than the $\overline{C}_{p,o}$ values over a substantial portion of the flap, and, as discussed in the main body of this report, results in a negative incremental normal force.

Pressure-coefficient distributions for other values of y/d_e for the conditions of figure 15 differed from those presented primarily in the maximum value of $C_{p,j}$ obtained. Otherwise, the distributions were of the same general shape as those presented. This can be seen in figure 16 where an isometric view of the pressure-coefficient distribution on the flap for $p_e/p_1 = 2.29$, $\epsilon = 0^o$, and $\alpha = 5^o$ is shown. This pressure-coefficient map is presented solely as an aid in visualizing the flow field downstream of the nozzle exits. As such, a "reflection" of the coefficients determined from measured pressures has been applied to the uninstrumented portion of the flap. The picture drawing portion of the hypersonic aerodynamics program, described in reference 6, was used to produce the map, and the small sketch at the upper left-hand corner of the figure shows the angle at which the flow field (and model) is being viewed in figure 16.

Average spanwise pressure coefficients $\overline{C}_{p,j}$ are shown in figure 17 for $p_e/p_1 \approx 2.0$ with the model at three angles of attack. Since p_e/p_1 is about the same for each angle of attack in this figure, the nozzle exit pressure, and, therefore, the pressure coefficient based on p_∞, increases with increasing α. Computing flap pressure coefficients on the basis of underwing conditions rather than free-stream conditions shows the effect of α on the data for a constant value of nozzle pressure ratio. This was done for the data of figure 17, and the results are shown in figure 18 for $\epsilon = 0^o$ and 4^o. Although p_e/p_1 is not exactly constant with α in figure 18, only a small difference in $(\overline{C}_{p,j})_1$ for the three angles of attack is noted. Since M_1 varied from 6 for $\alpha = 0^o$ to about 4.6 for $\alpha = 10^o$, this result indicates that external Mach number is not a primary variable and suggests that quiescent air tests may be feasible for preliminary parametric investigations of hypersonic jet interference effects provided the initial plume contours that would exist with external flow are simulated by adjustment of nozzle pressures or Mach number for the quiescent air tests.

Airplane Model Pressure-Coefficient Distributions

Model without inlet-nozzle section.- Engine-off pressure coefficient distributions on the airplane model for each row of pressure orifices are presented in figure 19 for an angle of attack of 5^o. As for the flat-plate model, these data are typical of those obtained for other angles of attack. The decrease in $C_{p,o}$ downstream of the nozzle

exit plane noted in figure 19 for stations $y/d_e = 0$ to 1.687 results from the contour of the model undersurface in this region. Outboard of $y/d_e = 1.687$, the model surface is relatively flat downstream of the nozzle exit plane.

The underwing reference pressure p_1 was established from the engine-off pressure-coefficient data as the pressure corresponding to the coefficient at $y/d_e = 0$ and $x/d_e = 0.125$. This is essentially the pressure existing on the model surface in the nozzle exit plane across the width of the inlet-nozzle section.

Model with $\gamma_e = 1.26$ asymmetric nozzles.- Pressure-coefficient distributions on the model undersurface along the center line of the inlet-nozzle section $(y/d_e = 0)$ and along the center line of one of the inboard nozzles are shown in figure 20 for an angle of attack of 5^o. The distributions follow the same pattern noted for the flat-plate model with axisymmetric nozzles, and the discussion pertaining to the flat-plate model is applicable here for the airplane model. The decrease in $C_{p,j}$ downstream of $x/d_e = 3$ in figure 20 results from a combination of the model contour and the expansion waves from the lower lip of the nozzle.

Figure 21 presents spanwise pressure-coefficient distribution for six stations downstream of the nozzle exit plane for a model angle of attack of 5^o. Because of the curvature of the model surface (and the inlet-nozzle section), the tangent point between the nozzle exit and the model surface does not lie on the nozzle center line in a plan-view projection of the model. This fact was overlooked in the design of the model so that the rows of orifices at $y/d_e = 1.125$ and 1.687 do not correspond with the rows at $y/d_e = 0$ and 0.563 from a symmetry standpoint. Therefore, the distributions in figure 21 have been faired to account for the discrepancy in location of the orifice rows. Closer spanwise spacing of the orifices was desirable on both models, but facility limitations restricted the number of pressure measurements that could be made.

The observations to be made from figure 21 are the same as those that can be noted in the pressure-coefficient map for the flat-plate model (fig. 16); that is, the high pressure region centered at the nozzle exit quickly switches to the region between the nozzles and remains between the nozzles for about 2 nozzle diameters downstream of the exit plane. Beyond 2 nozzle diameters, the pressure peaks start to disappear until, around 3 exit diameters downstream, the pressure is essentially constant across the nozzle flow.

Flat-Plate Model Aerodynamic Data

Incremental normal-force coefficient due to nozzle flow.- Incremental normal-force coefficients $(C_{N,j} - C_{N,o})$ resulting from the action of the nozzle flow on the flap surface of the flat-plate model are shown in figure 22(a) for the 2-D nozzle configuration and in figure 22(b) for the axisymmetric nozzle configuration. Note that $C_{N,j}$ is defined as

acting normal to the flap surface. The data points for $p_e/p_1 = 1$, 1.5, 2, 3, and 4 shown in these figures were obtained from curves faired through the experimental data points of plots of $C_{N,j}$ against nozzle pressure ratio. The calculated variation of the incremental normal-force coefficient with angle of attack and nozzle pressure ratio indicated by the dashed lines in figure 22(a) (2-D nozzles) was obtained from a simplified model of the flow over the flap surface which is discussed subsequently.

Calculations based on the simplified flow model adequately predict the incremental normal-force coefficients of the 2-D nozzle configuration for the test range of α, ϵ, and nozzle pressure ratio since momentum forces due to the nozzle flow are essentially accounted for in the flow model. Discrepancies noted earlier between calculated and experimental pressure-coefficient distributions are not significant insofar as the overall normal force is concerned.

Prediction of the incremental normal-force coefficient for the flat-plate model with axisymmetric nozzles (fig. 22(b)) was not as good at the high and low nozzle pressure ratios as that for the 2-D nozzle configuration. This result was not unexpected since the nozzle flow downstream of the axisymmetric nozzle exits is complex and not as readily simplified with generalized assumptions.

Effect of nozzle-exit ratio of specific heats γ_e.- Incremental normal-force coefficients for the two values of γ_e investigated on the flat-plate model are presented as a function of nozzle pressure ratio in figure 23 for $\epsilon = 0^o$ and 4^o at $\alpha = 0^o$. At a given pressure ratio, decreasing γ_e from 1.4 to 1.26 increases the incremental normal-force coefficient a significant amount. The magnitude of this effect of γ_e is open to question because of the uncertainty in the value of p_e. Pressure surveys across the nozzle exits were lost because of an instrumentation failure. The nozzle calibrations obtained for the airplane model nozzles were used to calculate the exit static pressures for the flat-plate model. Although the nozzle coordinates were nominally the same for both nozzles, small variations in nozzle contours due to machining tolerances can cause significant differences between the calibrations and affect the values of p_e. The trend of increasing normal force with decreasing γ_e noted in figure 23 is in agreement with data presented in reference 7. Reference 7 also shows that there is little change in normal force as γ_e is decreased below about 1.28.

Effect of nozzle pressure ratio on flap center-of-pressure location.- Pitching-moment coefficient data for the flat-plate model are presented indirectly in figure 24 as a variation of flap center-of-pressure location with nozzle pressure ratio. The center-of-pressure location is given in terms of nozzle heights for the 2-D nozzle configuration (fig. 24(a)) and in terms of nozzle diameters for the axisymmetric nozzle configuration (fig. 24(b)). A calculated variation of x_{cp} with nozzle pressure ratio is also shown for $\alpha = 5^o$ in figure 24(a).

APPENDIX B

The center-of-pressure location moves towards the nozzle exit as p_e/p_1 increases for those conditions for which $C_{N,j}$ is positive over the range of pressure ratios. When $C_{N,j}$ reverses sign for certain conditions, a discontinuity occurs in the curve where $C_N = 0$. The differences noted between experimental and calculated values of x_{cp}/h_e or x_{cp}/d_e reflect the differences between experimental and calculated pressure-coefficient distributions noted previously. Although the differences between experimental and calculated pressures are masked in the normal-force coefficient, they are reflected to a certain extent in the pitching-moment coefficient.

Flow Model and Calculation Procedures

The flow model used in calculating aerodynamic forces on the flat-plate model with the 2-D nozzle is shown in figure 25. The assumed longitudinal distribution of pressures on the flap surface downstream of the nozzle exit is shown in figure 25(a), and the assumed spanwise distribution of pressures is shown in figure 25(b). Although impingement on the model surface of the expansion waves from the lower edge of the nozzle causes a decrease in surface pressures over a finite distance (fig. 14), investigation showed that replacing the expansion fan by an average expansion wave (and effecting an instantaneous decrease in surface pressure at the impingement point of this single wave) yielded essentially the same force on a longitudinal strip as obtained by considering an expansion fan. A similar situation was found to exist for the expansion waves from the sides of the 2-D nozzle. That is, the force on a spanwise strip obtained by considering the side expansion fans and external shocks was closely matched by assuming that the pressure was constant across the width of the inlet-nozzle section and equal to the center-line pressure (fig. 25(b)). With the simplified distributions, the normal force on the flap surface for $\epsilon = 0^o$ (for example) with nozzle flow is

$$\text{Normal force} = p_e(wx) + p_3(wx') \tag{B1}$$

Expressing the normal force in coefficient form, the incremental normal-force coefficient with nozzle flow for $\epsilon = 0^o$ is then

$$C_{N,j} - C_{N,o} = \frac{2w}{\gamma_\infty M_\infty^2 A_{ref}} \left\{ \left[x\left(\frac{p_e}{p_\infty} - 1\right) + x'\left(\frac{p_3}{p_\infty} - 1\right) \right] - \left[(x + x')\left(\frac{p_1}{p_\infty} - 1\right) \right] \right\} \tag{B2}$$

where

$$x = \frac{h}{\tan}$$

and the angle ϕ (defined in fig. 25) is a function of M_e and M_2. Pitching-moment coefficients (about the axis through the juncture between the nozzle exit plane and the model surface) were then calculated from the following expression:

$$C_{m,j} = -\frac{1}{l_{ref}}\left[C_{N,e}\frac{x}{2} + C_{N,3}\left(x + \frac{x'}{2}\right)\right] \tag{B3}$$

The procedure for calculating forces on the axisymmetric nozzle configurations was to modify, in two ways, the results calculated for the same configurations by assuming that the nozzle flow was two dimensional. First, the radial dissipation of the axisymmetric nozzle flow momentum was accounted for by considering the upward vertical component of the momentum relative to the total momentum. That is,

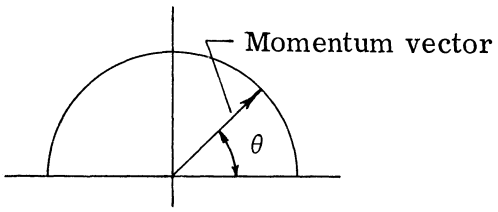

$$\frac{\text{Vertical momentum}}{\text{Total momentum}} = \frac{\int_0^{\pi/2} (\text{Momentum})\sin\theta\, d\theta}{\int_0^{\pi/2} (\text{Momentum})\, d\theta} = \frac{2}{\pi}$$

so that initially

$$(C_{N,j} - C_{N,o})_{\text{axisymmetric}} = \frac{2}{\pi}(C_{N,j} - C_{N,o})_{2\text{-D}}$$

The second modification of the 2-D results was applied to account for the difference in the contact, or footprint, areas between the two types of nozzle flows on the flap surface. At low nozzle pressure ratios (<2.0), the ideal footprint area of the axisymmetric nozzle flow is small while the 2-D nozzle flow is in complete contact with the flap surface. To account for the effect of this difference in footprint areas on the normal-force coefficient, it was assumed that the flap surface area not in contact with the nozzle flow was subject to a base pressure $\left(C_{p,b} = -1/M_e^2\right)$. The area on which this pressure acted was obtained by first calculating the plume contour at a given pressure ratio and determining the footprint area from the plume shape. The area in question is the difference between the plume contact area for 2-D nozzles $A_{2\text{-D}} = w(x + x')$ (fig. 25) and the total footprint

area A_{foot} for the four nozzles. The plume shapes were calculated by the empirical method of reference 8 which gives a close approximation of the shape of the initial portion of a plume in quiescent air. (See ref. 9, also.) The area between the footprints becomes small at $p_e/p_1 = 1.5$,

$$\frac{A_{2\text{-}D} - A_{foot}}{A_{2\text{-}D}} = 0.06$$

and negligible (0.01) for pressure ratios equal to or greater than 2 when compared with a value of 0.21 for $p_e/p_1 = 1$. Finally,

$$\left(C_{N,j} - C_{N,o}\right)_{3\text{-}D} = \frac{2}{\pi}\left(C_{N,j} - C_{N,o}\right)_{2\text{-}D} + C_{p,b}\frac{A_{2\text{-}D} - A_{foot}}{A_{ref}} \tag{B4}$$

At $p_e/p_1 = 1.0$, $\left(C_{N,j} - C_{N,o}\right)_{2\text{-}D} = 0$ so that the calculated incremental normal force for the axisymmetric nozzle case (3-D) is equal to the force acting on the area between the plume footprints. Since the pressure assumed to be acting on this area is probably less than the actual pressure (because of flow recirculation and pressure feedback from interference between adjacent nozzle flows), the calculated incremental normal-force coefficient is more negative than noted for the data. Although at $p_e/p_1 = 1$ there should be no pluming of the nozzle flow and the plume footprint should then be a line on the flap surface, the nozzle flow next to the flap is expanding to the assumed base pressure; therefore, the ratio of nozzle exit pressure to base pressure is about 3.3.

APPENDIX C

ANALYTIC PROCEDURE FOR BREGUET FACTOR CALCULATIONS

Jet Interference

The cruise range of an airplane is given by

$$R = \int_{t_i}^{t_f} V \, dt = -\int_{W_i}^{W_f} V \frac{dW}{\dot{w}_{fuel}} \tag{C1}$$

where

t	time
V	velocity
W	instantaneous airplane weight
$\dot{w}_{fuel}$	fuel flow rate

and subscripts i and f refer to initial and final values, respectively.

The range parameter for an airplane using jet interference is calculated as follows. Assume that the gross thrust $C_{F,g}$ and ram drag $C_{D,R}$ are both alined with the wing undersurface which is at an angle α to the free-stream velocity. The net thrust $C_{F,N}$ is $C_{F,g} - C_{D,R}$ and is also alined with the wing undersurface.

The diagram of forces acting on the airplane during cruise is

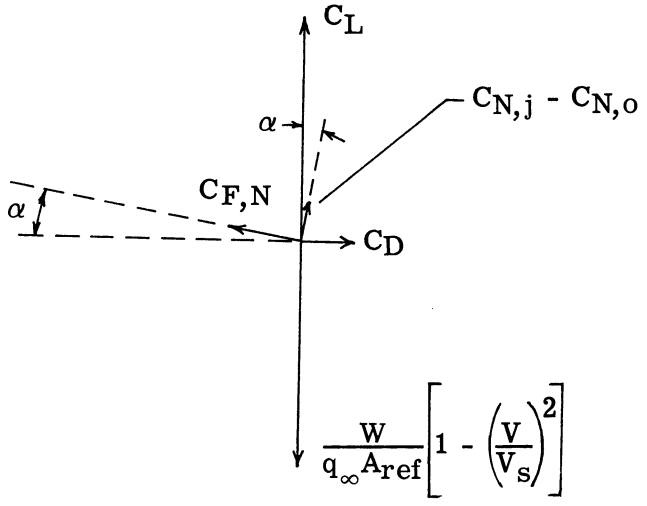

where V_S is the satellite velocity. (See "Symbols" in main body of report for definition of symbols not defined in this appendix.) Summing forces in the lift and drag directions yields

$$C_D \frac{L}{D} + C_{F,N} \sin \alpha + \left(C_{N,j} - C_{N,o}\right)\cos \alpha = \frac{W}{q_\infty A_{ref}}\left[1 - \left(\frac{V}{V_s}\right)^2\right] \tag{C2}$$

and

$$C_{F,N} \cos \alpha = \left(C_{N,j} - C_{N,o}\right) \sin \alpha + C_D \tag{C3}$$

Combining equations (C2) and (C3) and rearranging give

$$C_{F,N}\left\{\sin \alpha + \frac{L}{D}\left[\cos \alpha + \frac{C_{N,j} - C_{N,o}}{C_{F,g}} \frac{C_{F,g}}{C_{F,N}}\left(\frac{\cos \alpha}{L/D} - \sin \alpha\right)\right]\right\} = \frac{W}{q_\infty A_{ref}}\left[1 - \left(\frac{V}{V_s}\right)^2\right] \tag{C4}$$

and

$$F_N = C_{F,N} q_\infty A_{ref} = \dot{w}_{fuel} I_{sp} \tag{C5}$$

where I_{sp} is specific impulse.

Combining equations (C1), (C4), and (C5) yields

$$R = -\int_{W_i}^{W_f} I_{sp} V \left\{\sin \alpha + \frac{L}{D}\left[\cos \alpha + \frac{C_{N,j} - C_{N,o}}{C_{F,g}} \frac{C_{F,g}}{C_{F,N}}\left(\frac{\cos \alpha}{L/D} - \sin \alpha\right)\right]\right\} \left\{\frac{dW}{W\left[1 - \left(\frac{V}{V_s}\right)^2\right]}\right\} \tag{C6}$$

The Breguet factor (BF) is defined as

$$R = -\int_{W_i}^{W_f} BF \frac{dW}{W} \tag{C7}$$

Thus the Breguet factor for an airplane using jet interference effects is

$$BF = \frac{VI_{sp}}{1 - \left(V/V_s\right)^2}\left\{\sin\alpha + \frac{L}{D}\left[\cos\alpha + \frac{C_{N,j} - C_{N,o}}{C_{F,g}}\frac{C_{F,g}}{C_{F,N}}\left(\frac{\cos\alpha}{L/D} - \sin\alpha\right)\right]\right\} \tag{C8}$$

Note that, for an airplane with the engines mounted at the wing trailing edge so that no jet interference effects occur $\frac{C_{N,j} - C_{N,o}}{C_{F,g}} = 0$, the Breguet factor becomes

$$BF = \frac{VI_{sp}\left(\sin\alpha + \frac{L}{D}\cos\alpha\right)}{1 - \left(V/V_s\right)^2} \tag{C9}$$

Thrust Vectoring

Lift can be derived from a jet exhaust by vectoring the gross thrust through an angle η with respect to the free-stream velocity. Assume that the ram drag is alined with the wing undersurface and that the magnitude of the gross thrust is unaffected by vectoring. The force diagram for this case is

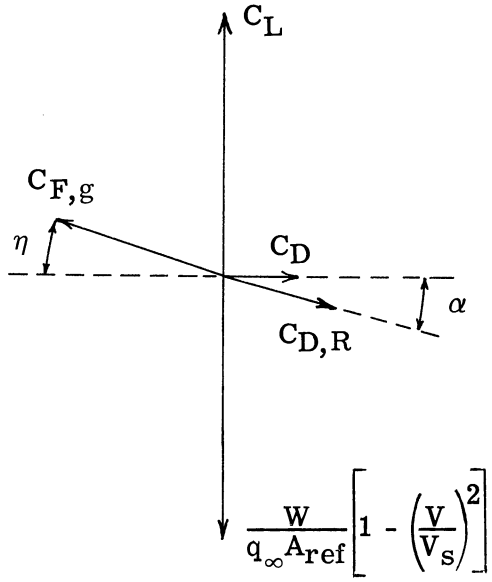

APPENDIX C

Let $\overline{C}_{F,N}$ be the net thrust coefficient that results when $\eta = \alpha$; then

$$\overline{C}_{F,N} = \left|C_{F,g}\right| - \left|C_{D,R}\right|$$

or

$$\left|\frac{C_{D,R}}{C_{F,g}}\right| = 1 - \left|\frac{\overline{C}_{F,N}}{C_{F,g}}\right| \tag{C10}$$

Summing forces in the lift and drag directions yields

$$C_D \frac{L}{D} + C_{F,g} \sin \eta - C_{D,R} \sin \alpha = \frac{W\left[1 - \left(V/V_s\right)^2\right]}{q_\infty A_{ref}} \tag{C11}$$

$$C_{F,g} \cos \eta - C_{D,R} \cos \alpha = C_D \tag{C12}$$

The relation between $\dot{w}_{fuel}$ and $\overline{C}_{F,N}$ is

$$\overline{C}_{F,N} q_\infty A_{ref} = \dot{w}_{fuel} I_{sp} \tag{C13}$$

where I_{sp} is the conventional specific impulse and is identical to the specific impulse used in equations (C5) and (C8).

Equations (C10), (C11), and (C12) can be combined to yield

$$\overline{C}_{F,N} q_\infty A_{ref} \frac{C_{F,g}}{\overline{C}_{F,N}}\left[\sin \eta + \frac{L}{D} \cos \eta - \left(1 - \left|\frac{\overline{C}_{F,N}}{C_{F,g}}\right|\right)\left(\sin \alpha + \frac{L}{D} \cos \alpha\right)\right] = W\left[1 - \left(\frac{V}{V_s}\right)^2\right] \tag{C14}$$

The gross thrust vector angle can be shown (ref. 5) to yield maximum range when

$$\tan \eta = \frac{1}{L/D}$$

Thus

$$\sin \eta = \left[(L/D)^2 + 1\right]^{-1/2} \qquad \text{and} \qquad \cos \eta = \frac{L}{D}\left[(L/D)^2 + 1\right]^{-1/2} \tag{C15}$$

Using equations (C1), (C13), (C14), (C15) and the definition of Breguet factor (eq. (C7)) gives

$$BF = \frac{VI_{sp}}{\left[1 - (V/V_s)^2\right]}\left|\frac{C_{F,g}}{\overline{C}_{F,N}}\right|\left[\sqrt{\left(\frac{L}{D}\right)^2 + 1} - \left(1 - \left|\frac{\overline{C}_{F,N}}{C_{F,g}}\right|\right)\left(\sin \alpha + \frac{L}{D}\cos \alpha\right)\right] \tag{C16}$$

REFERENCES

1. Johnston, P. J.; Cubbage, J. M.; and Weidner, J. P.: Studies of Engine-Airframe Integration on Hypersonic Aircraft. AIAA Pap. No. 70-542, May 1970.

2. Kirkham, Frank S.; Cubbage, James M., Jr.; Vahl, Walter A.; and Small, William J.: Studies of Airframe—Propulsion-System Integration for Mach 6 Cruise Vehicles. NASA TN D-4128, 1967.

3. Penland, Jim A.; Edwards, Clyde L. W.; Witcofski, Robert D.; and Marcum, Don C., Jr.: Comparative Aerodynamic Study of Two Hypersonic Cruise Aircraft Configurations Derived From Trade-Off Studies. NASA TM X-1436, 1967.

4. Jarlett, F. E.: Performance Potential of Hydrogen Fueled, Airbreathing Cruise Aircraft. Vols. 1-4. Rep. No. GD/C-DCB66-004/1-4 (Contract NAS 2-3180), Gen. Dyn., Sept. 30, 1966.

5. Krase, W. H.: Thrust Deflection for Cruise. J. Aircraft, vol. 4, no. 2, Mar.-Apr. 1967, pp. 162-164.

6. Gentry, Arvel E.: Hypersonic Arbitrary-Body Aerodynamic Computer Program (Mark III Version). Vol. I – User's Manual. Rep. DAC 61552 (Air Force Contract Nos. F33615 67 C 1008 and F33615 67 C 1602), Douglas Aircraft Co., Apr. 1968. (Available from DDC as AD 851 811.)

7. Gopin, A. J.; and Margolin, E. L.: A Cold Gas, Short Duration Technique for High Altitude, Underexpanded Jet Exhaust Impingement Studies. NASA TN D-2943, 1965.

8. Latvala, E. K.: Spreading of Rocket Exhaust Jets at High Altitudes. AEDC-TR-59-11, DDC Doc. No. AD-215866, U.S. Air Force, June 1959.

9. Vick, Allen R.; Andrews, Earl H., Jr.; Dennard, John S.; and Craidon, Charlotte B.: Comparisons of Experimental Free-Jet Boundaries With Theoretical Results Obtained With the Method of Characteristics. NASA TN D-2327, 1964.

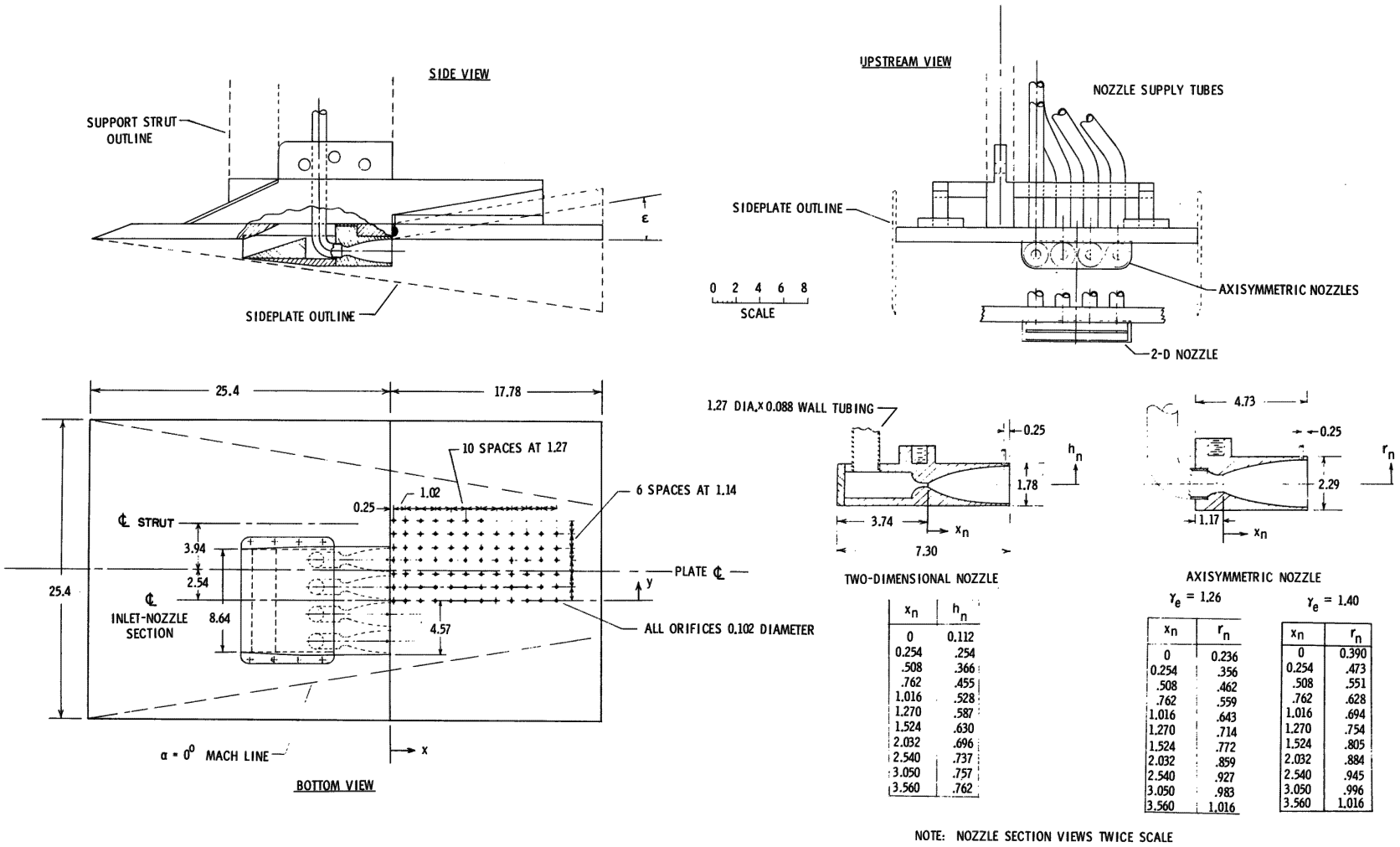

x_n	h_n
0	0.112
0.254	.254
.508	.366
.762	.455
1.016	.528
1.270	.587
1.524	.630
2.032	.696
2.540	.737
3.050	.757
3.560	.762

$\gamma_e = 1.26$

x_n	r_n
0	0.236
0.254	.356
.508	.462
.762	.559
1.016	.643
1.270	.714
1.524	.772
2.032	.859
2.540	.927
3.050	.983
3.560	1.016

$\gamma_e = 1.40$

x_n	r_n
0	0.390
0.254	.473
.508	.551
.762	.628
1.016	.694
1.270	.754
1.524	.805
2.032	.884
2.540	.945
3.050	.996
3.560	1.016

NOTE: NOZZLE SECTION VIEWS TWICE SCALE

(a) Drawing of flat-plate model including nozzle coordinates and pressure orifice locations. All dimensions are in cm.

Figure 1.- Flat-plate model.

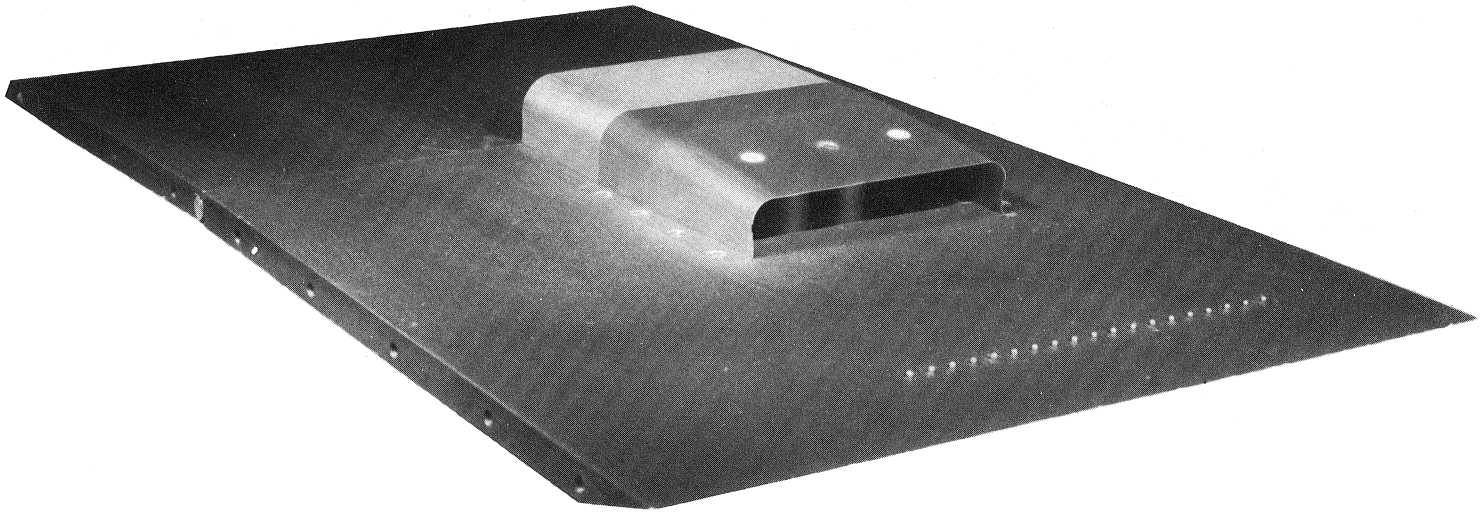

L-69-8473

(b) Three-quarter front view of model. $\epsilon = 2^{o}$; 1.19-mm-diameter spherical boundary-layer trips.

Figure 1.- Continued.

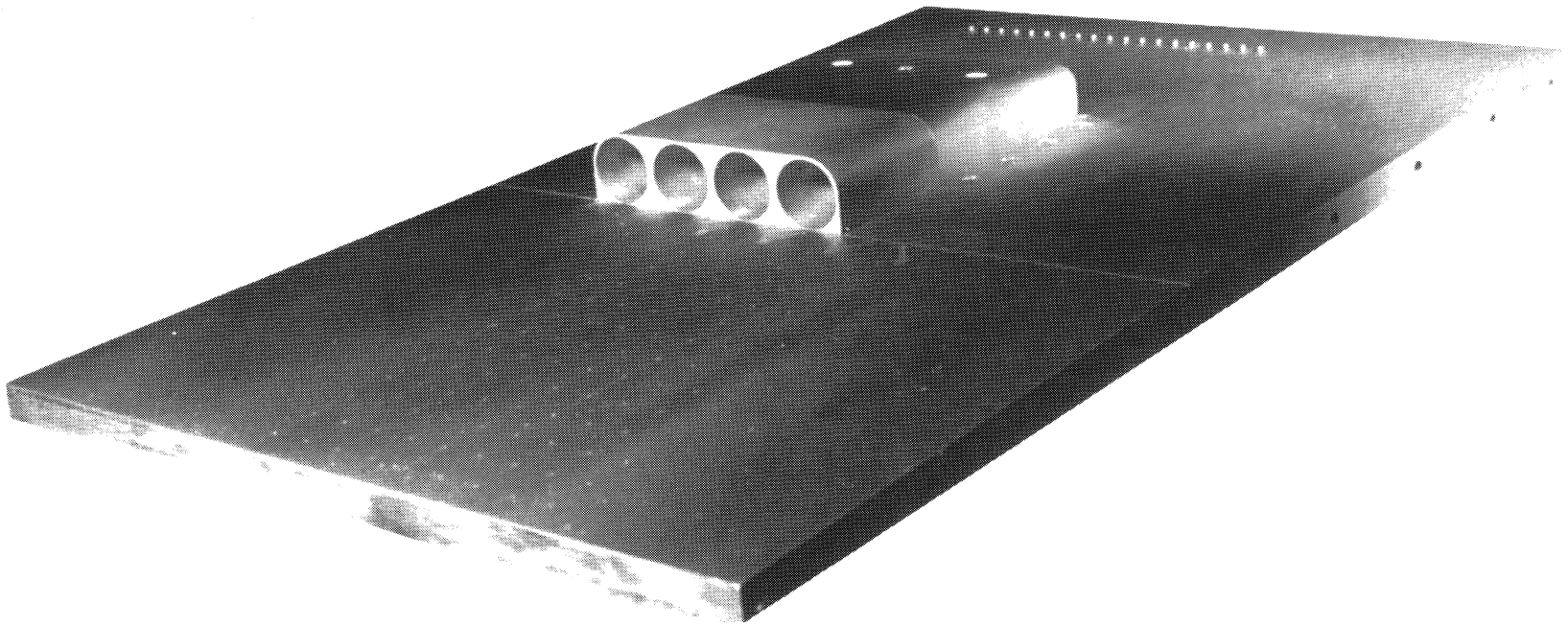

L-69-8474

(c) Three-quarter rear view of model. $\epsilon = 2^{o}$; $\gamma_e = 1.4$ axisymmetric nozzles.

Figure 1.- Concluded.

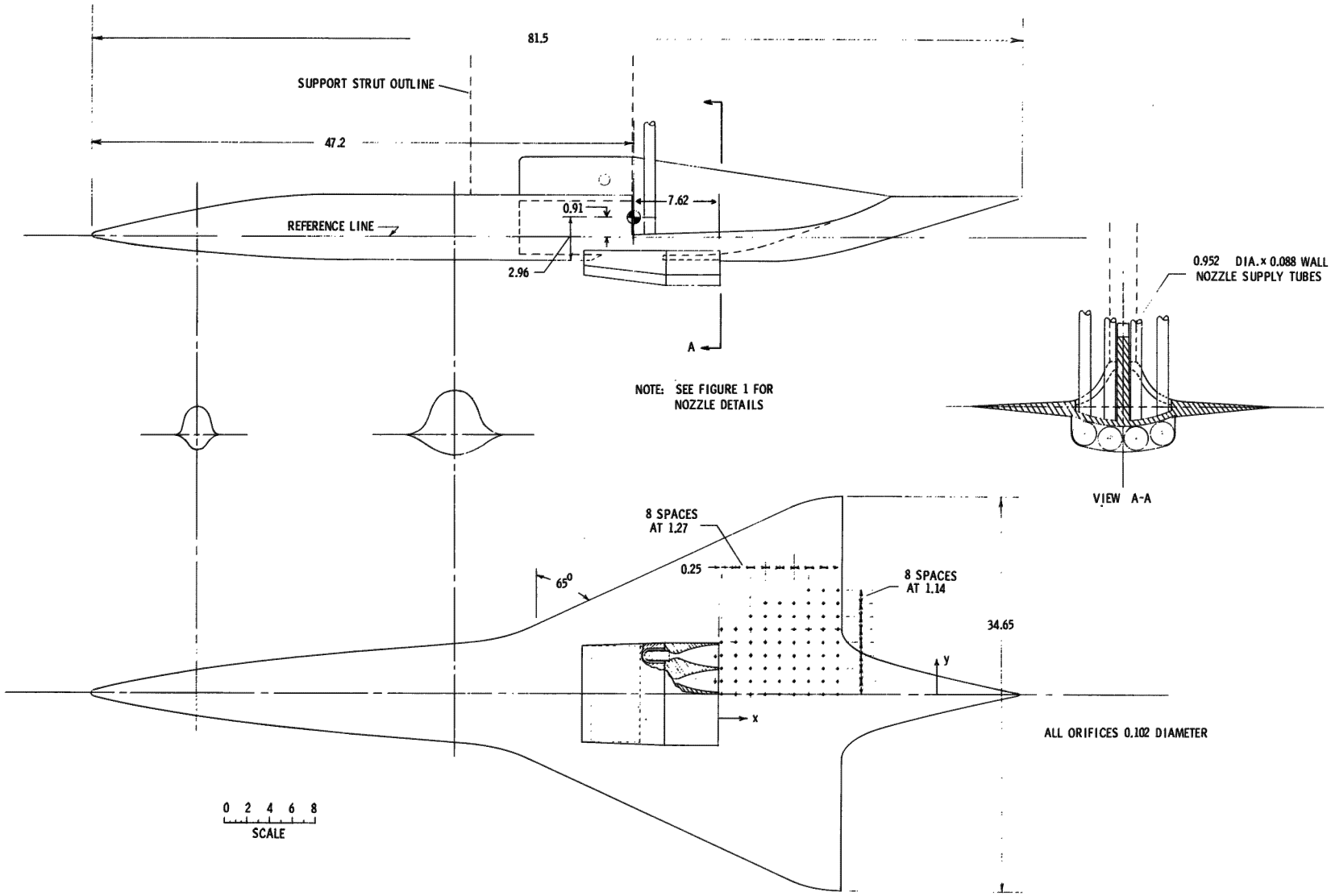

(a) Drawing of airplane model including pressure orifice locations. All dimensions are in cm.

Figure 2.- Airplane model.

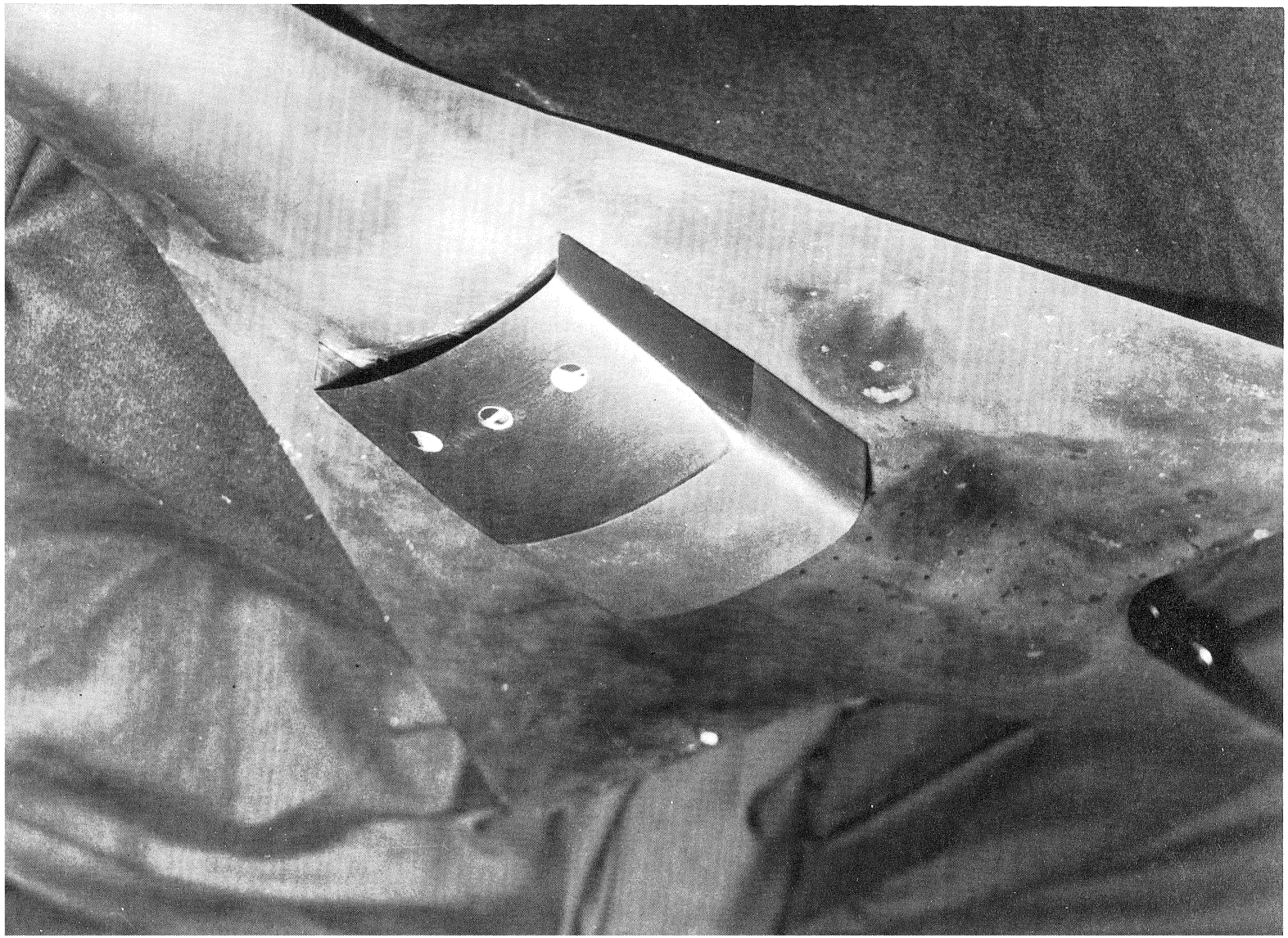

L-69-8476

(b) View of inlet-nozzle section and undersurface of model.

Figure 2.- Continued.

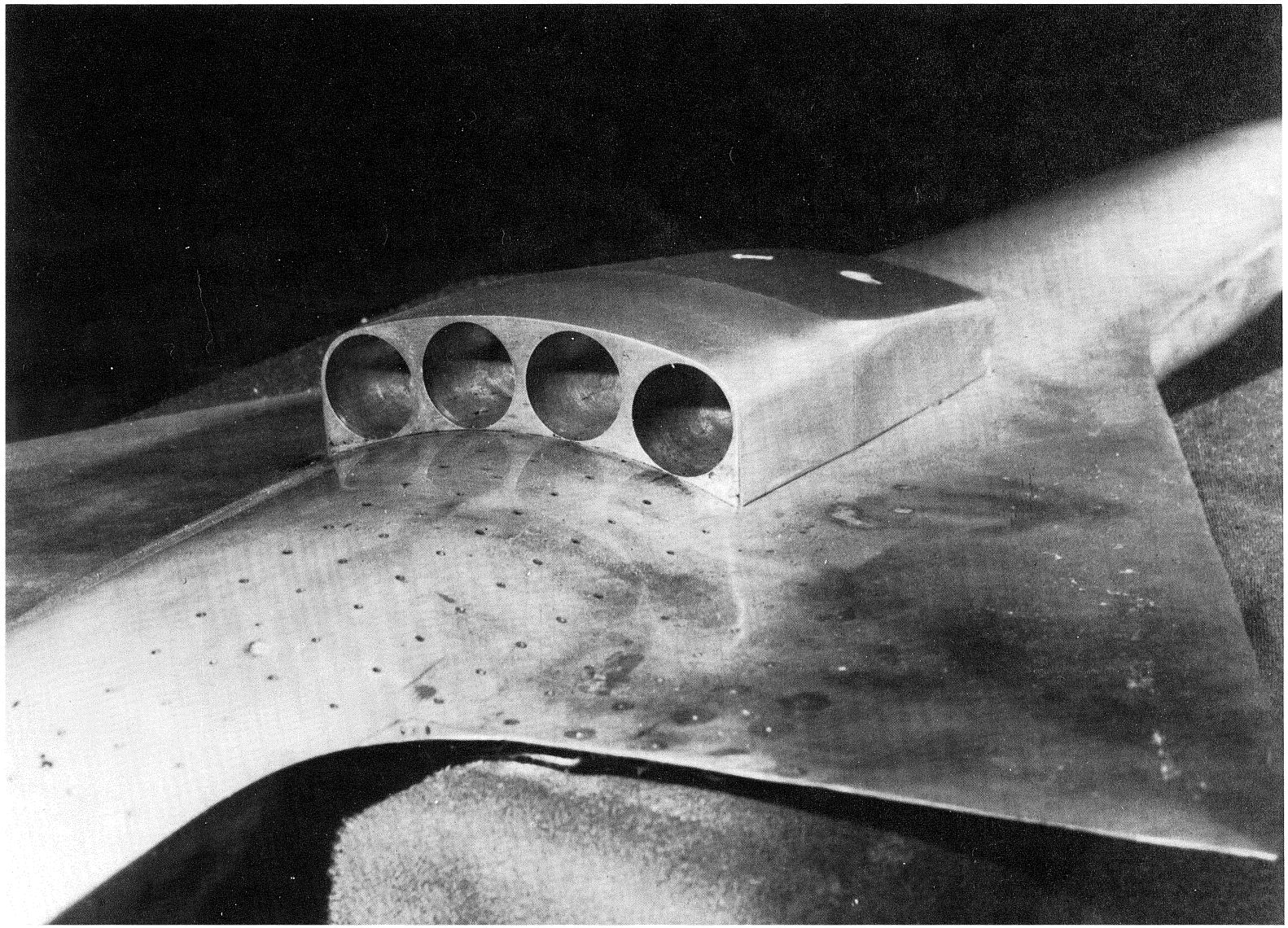

L-69-8475

(c) Rear view of inlet-nozzle section.

Figure 2.- Concluded.

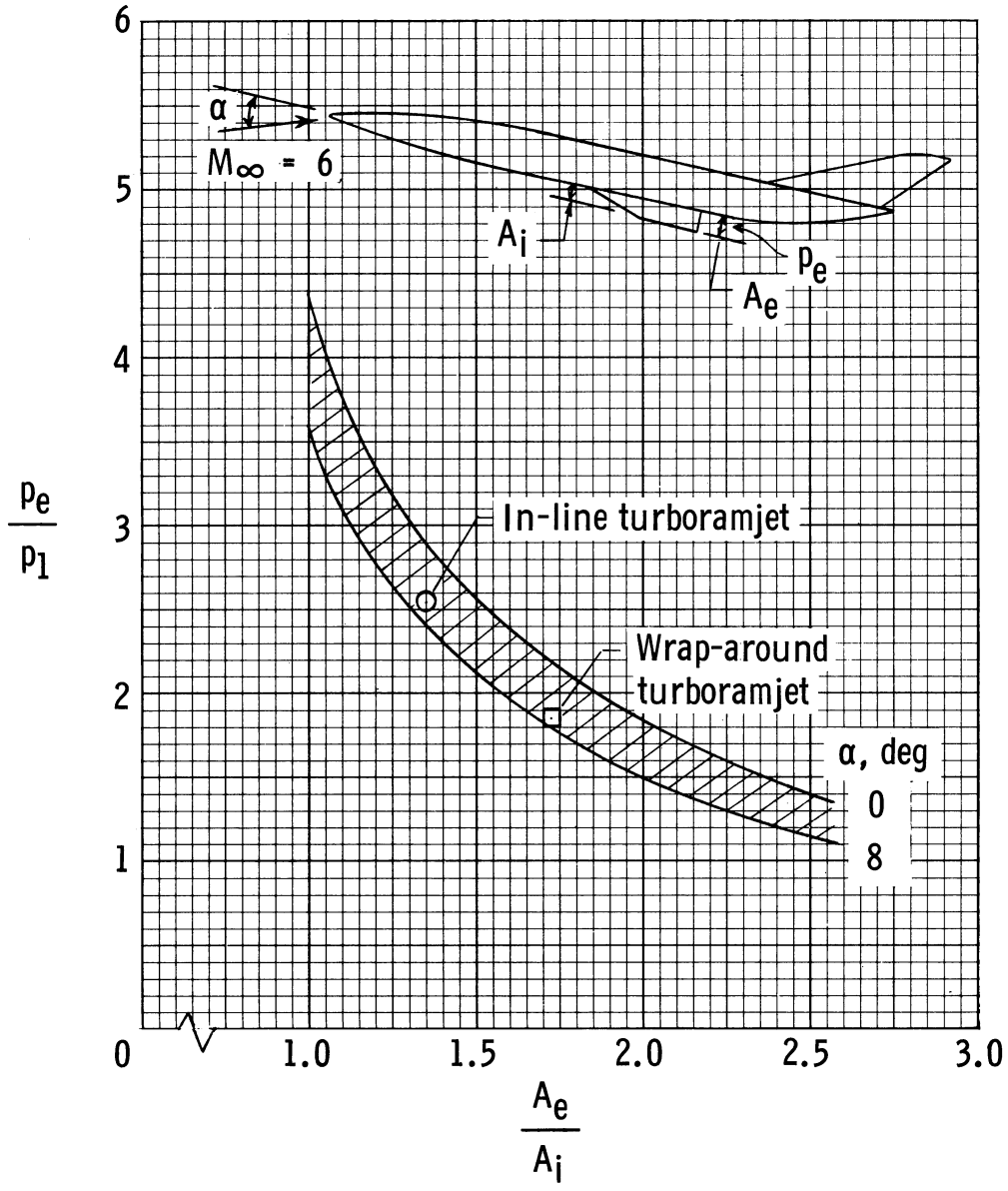

Figure 3.- Variation of nozzle pressure ratio with nacelle external expansion ratio for ramjet alone and for conditions typical of Mach 6 cruise operation.

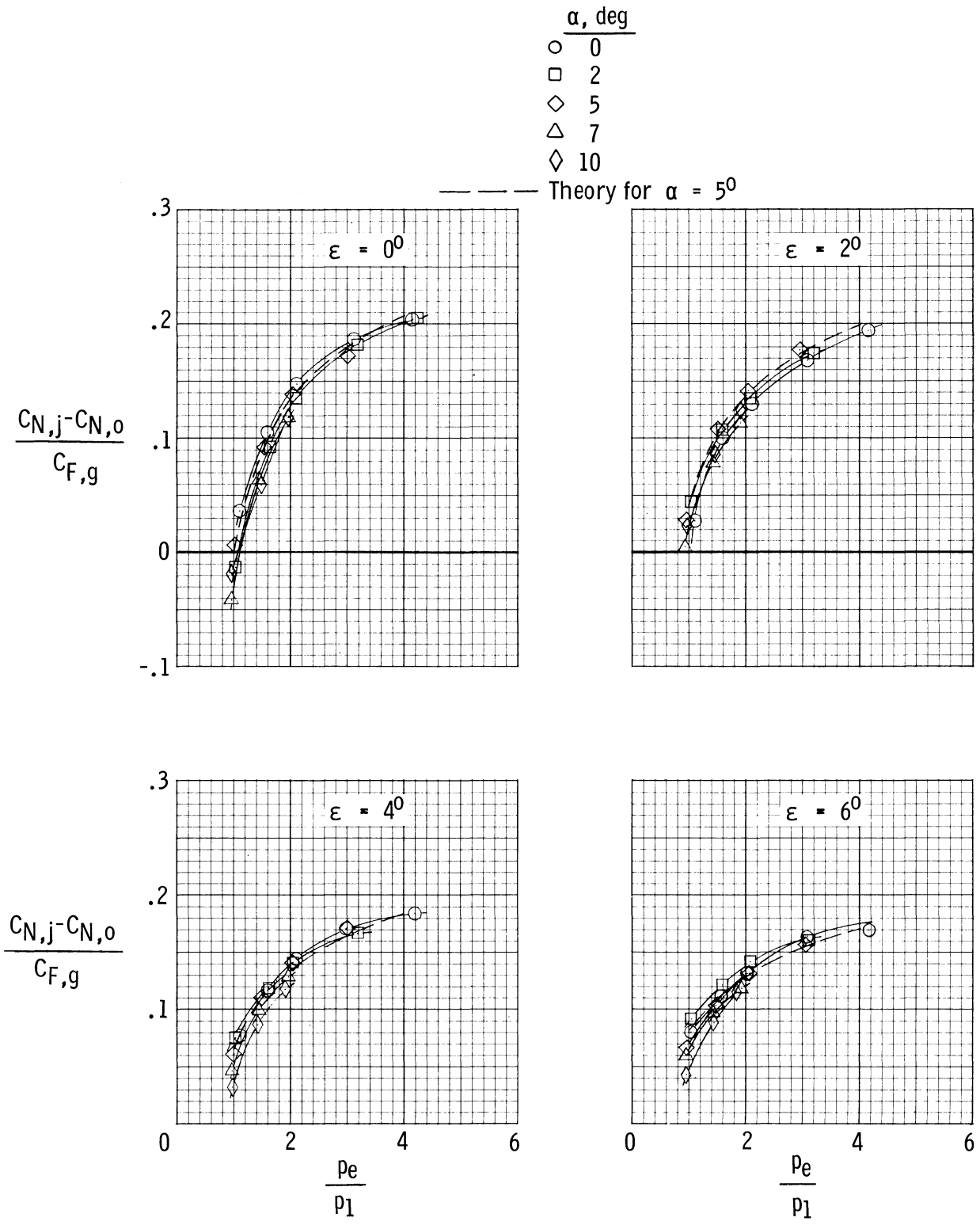

(a) 2-D nozzles.

Figure 4.- Ratio of incremental normal-force coefficient to nozzle gross thrust coefficient. $\gamma_e = 1.4$.

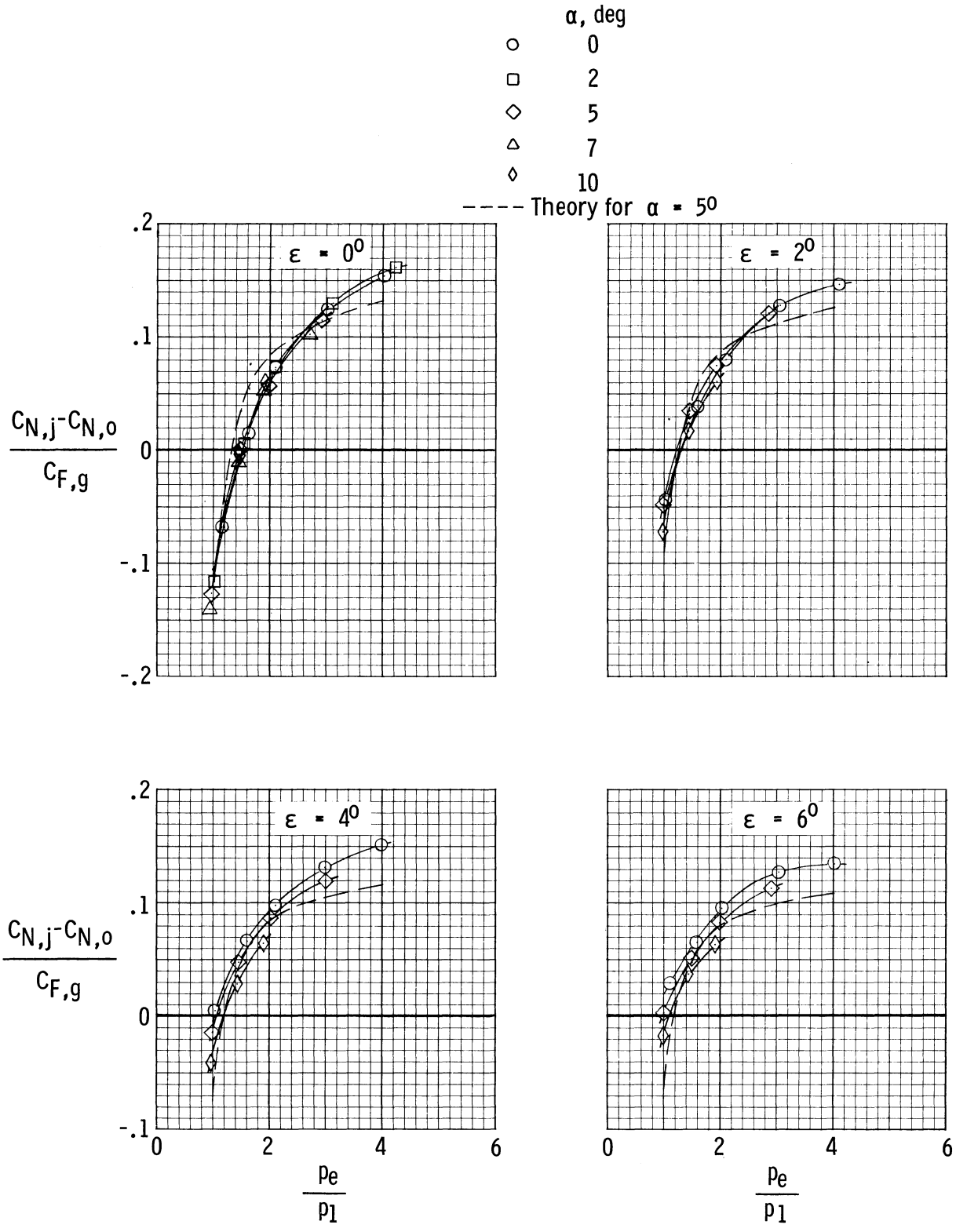

(b) Axisymmetric nozzles.

Figure 4.- Concluded.

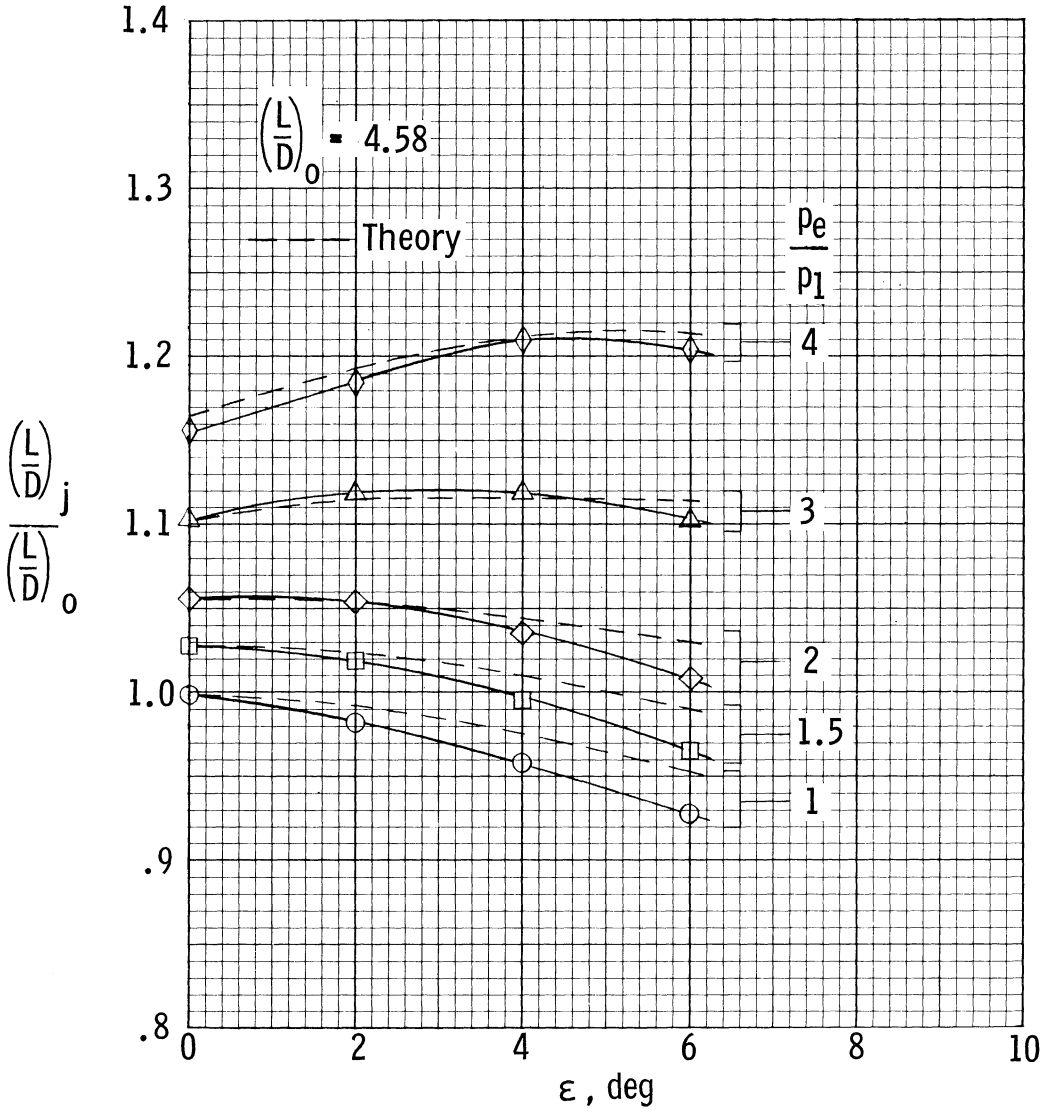

(a) 2-D nozzles.

Figure 5.- Effect of reflex angle on aerodynamic performance of flat-plate model. $\alpha = 5^{o}$; $\gamma_e = 1.4$; symbols used to identify faired values obtained from data.

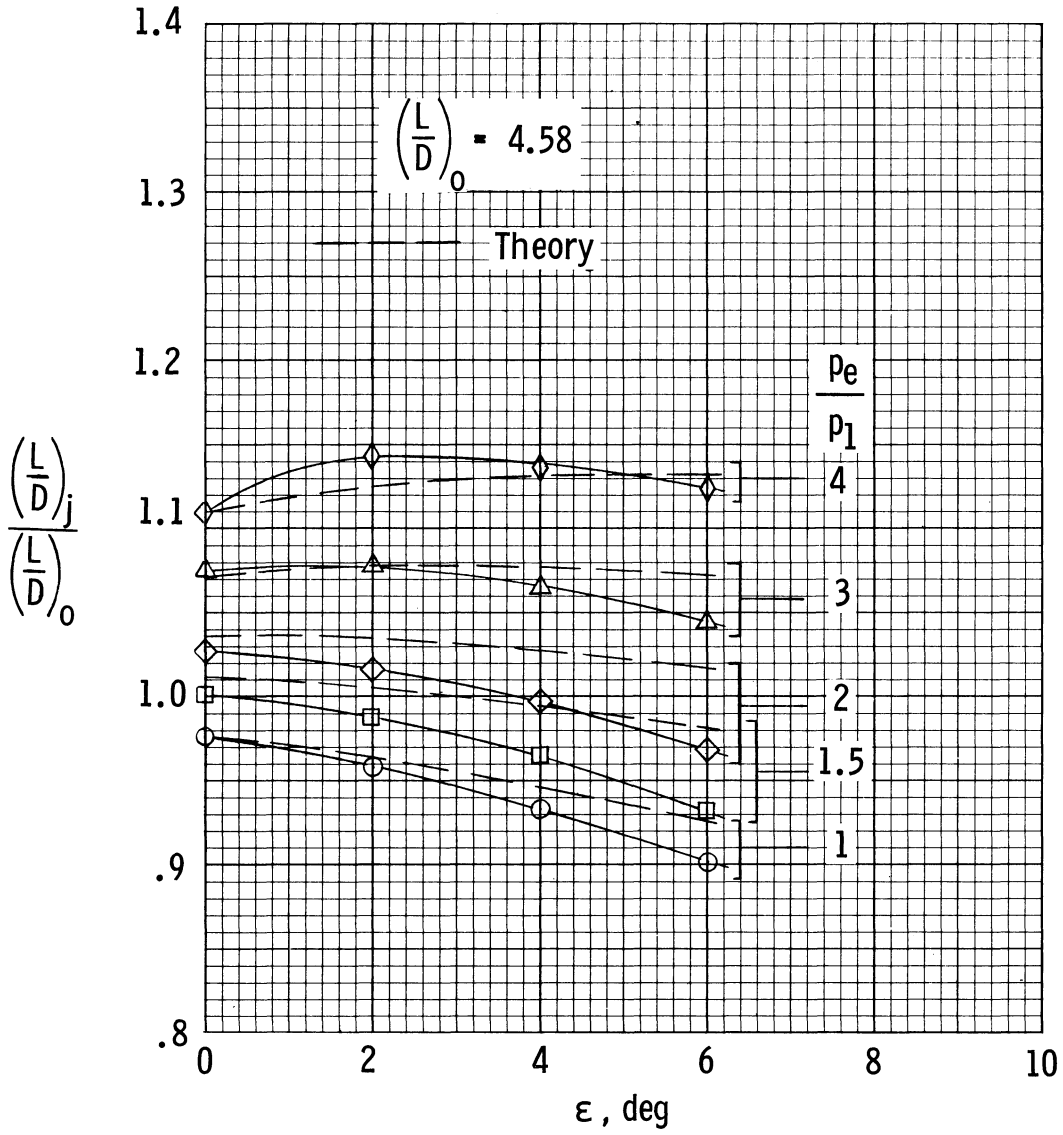

(b) Axisymmetric nozzles.

Figure 5.- Concluded.

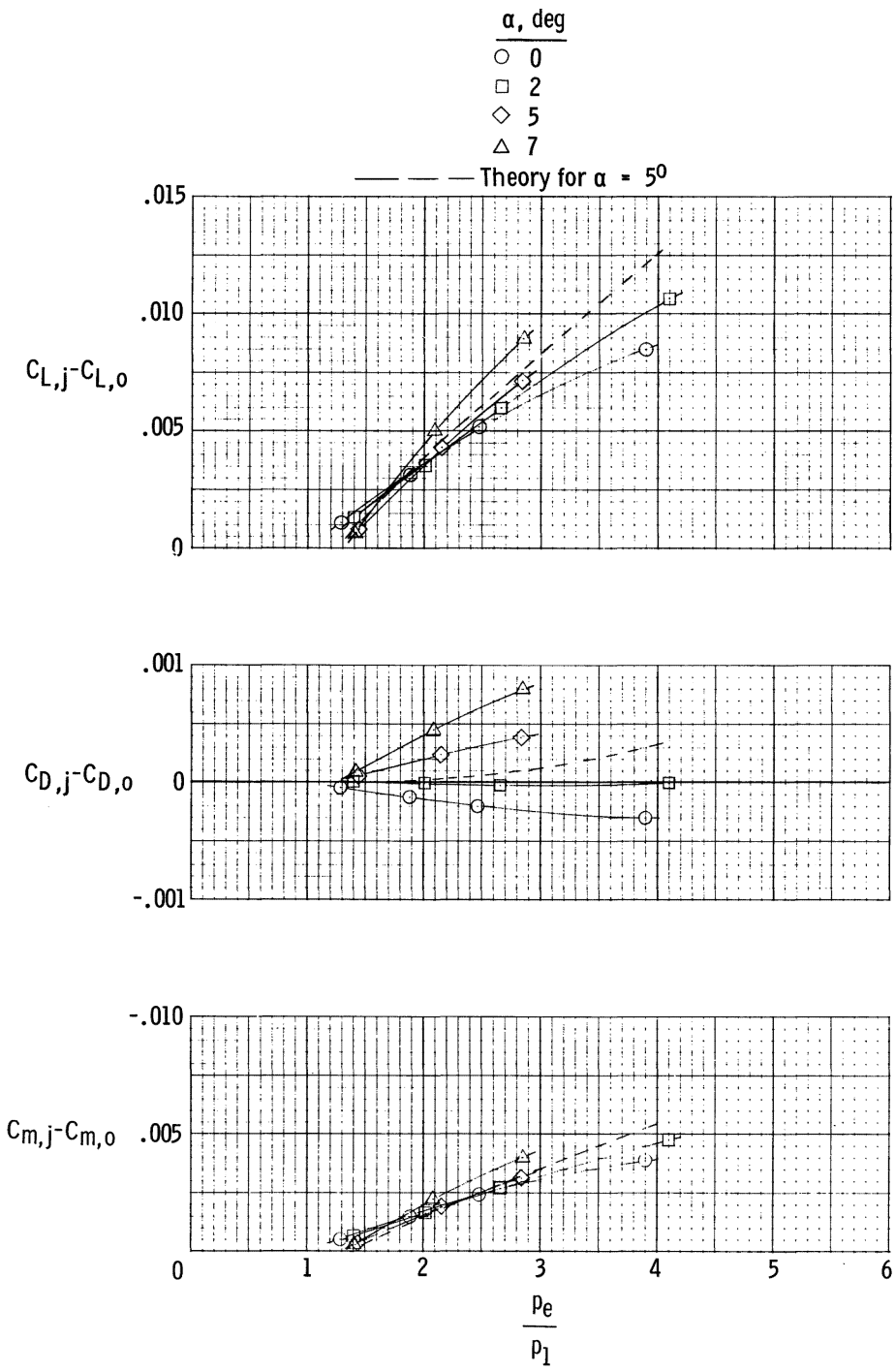

Figure 6.- Airplane model incremental lift, drag, and pitching-moment coefficients resulting from nozzle flow. A_{ref} = 734 cm^2; l_{ref} = 26.6 cm; γ_e = 1.26.

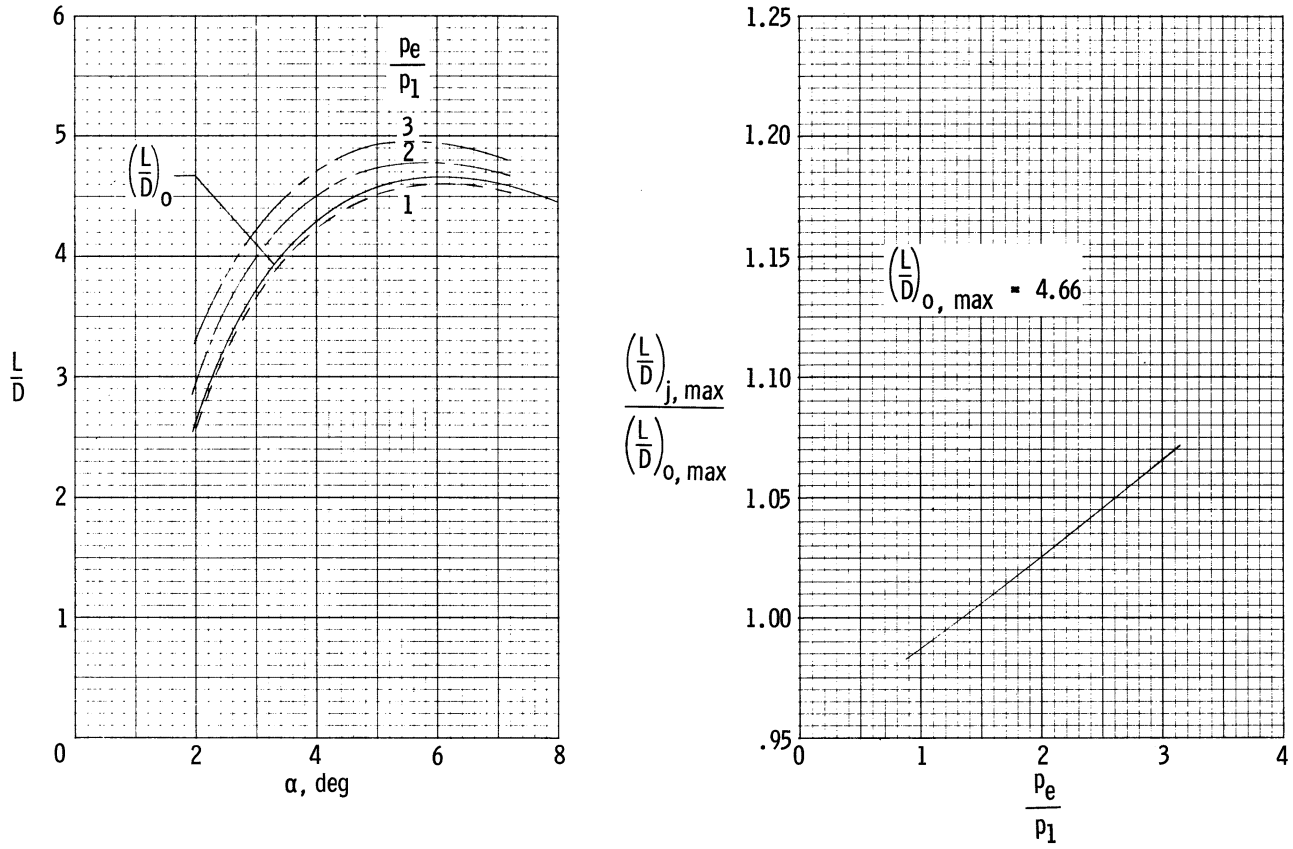

(a) Effect of jet interference on L/D. (b) Effect of jet interference on $(L/D)_{max}$.

Figure 7.- Effect of jet interference on aerodynamic performance of airplane model. $\gamma_e = 1.26$.

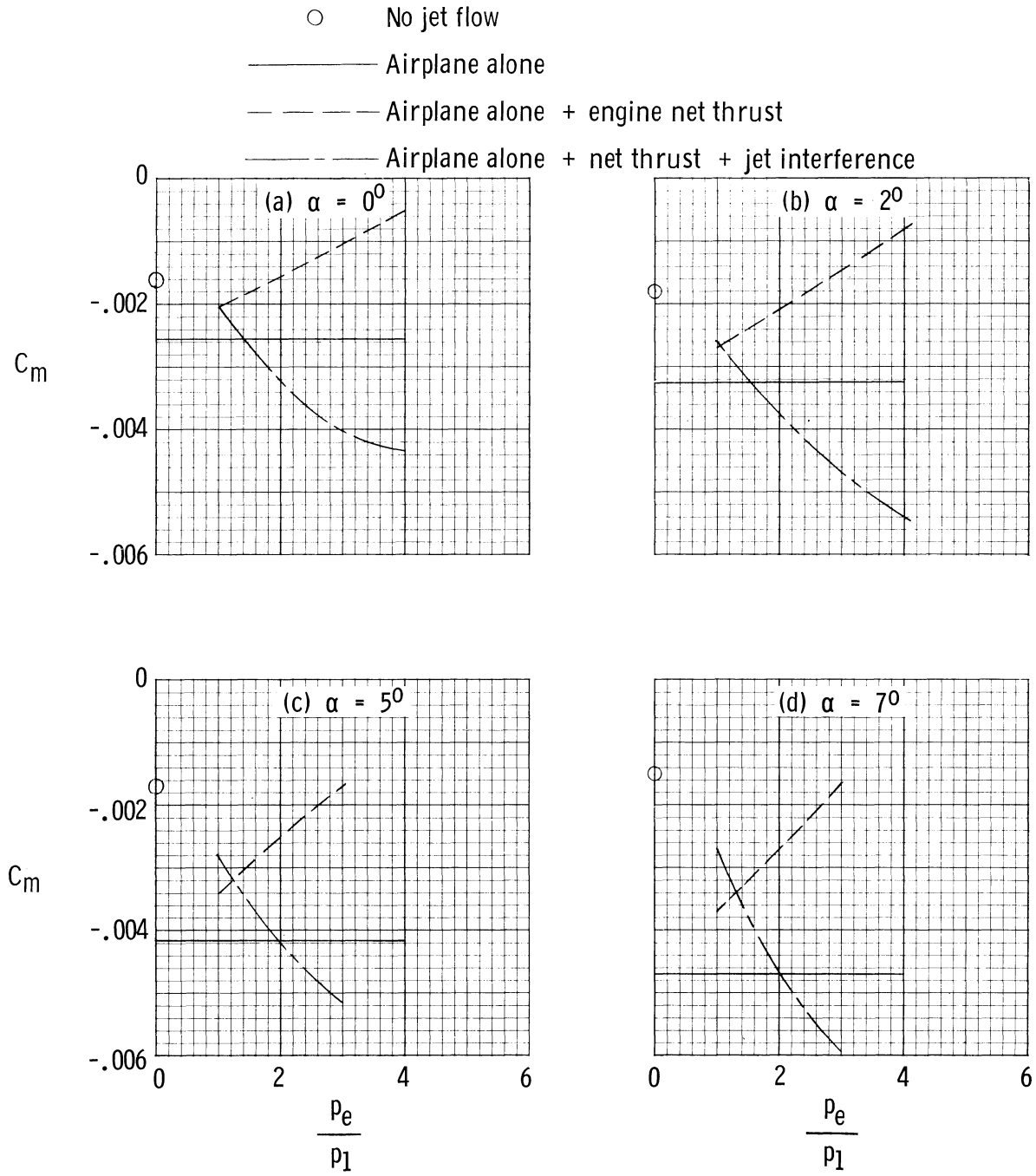

Figure 8.- Effect of net engine thrust and jet interference on airplane model pitching-moment coefficient. A_{ref} = 734 cm^2; l_{ref} = 26.6 cm; γ_e = 1.26.

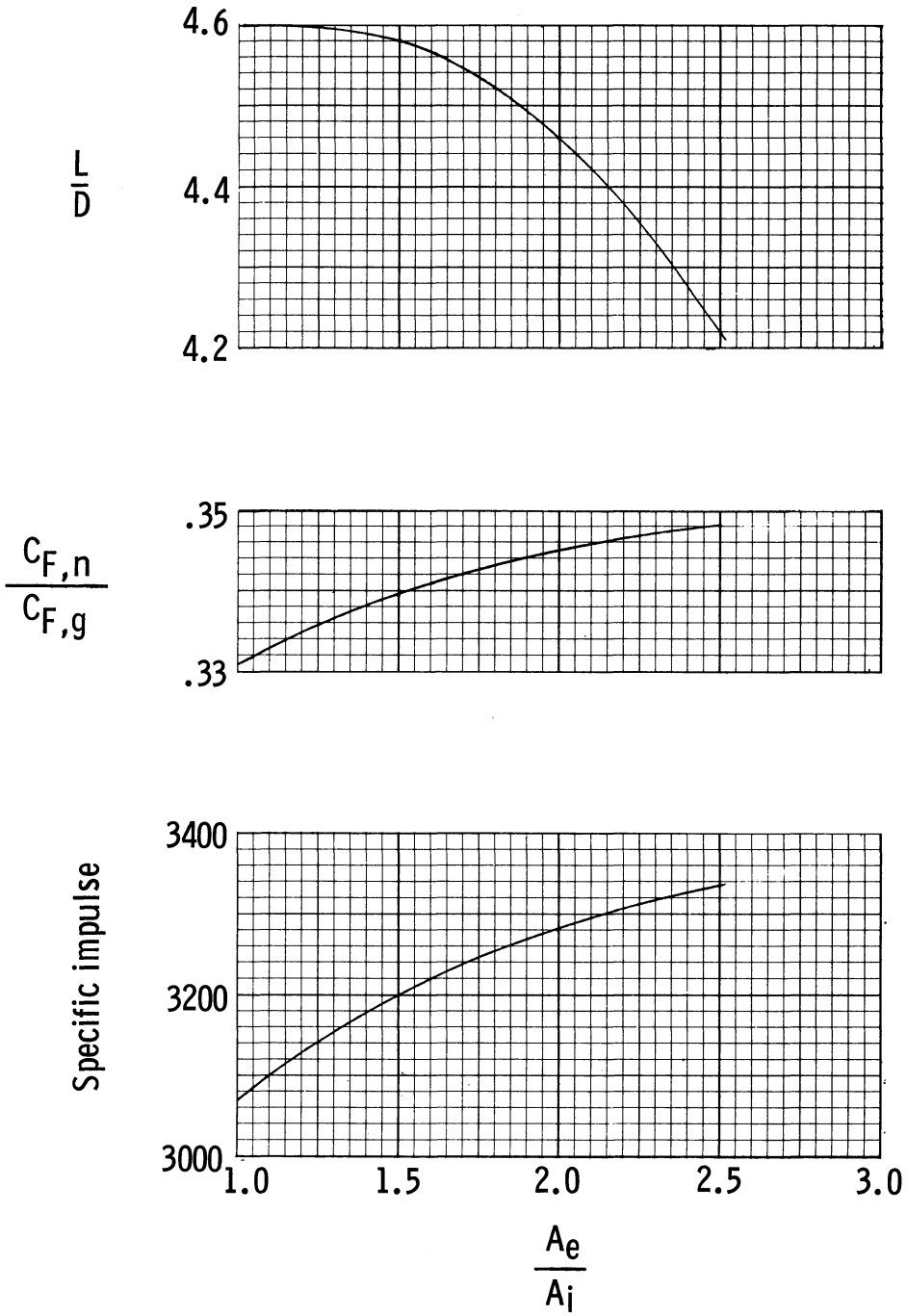

Figure 9.- Engine and aerodynamic parameters for Breguet factor calculation.

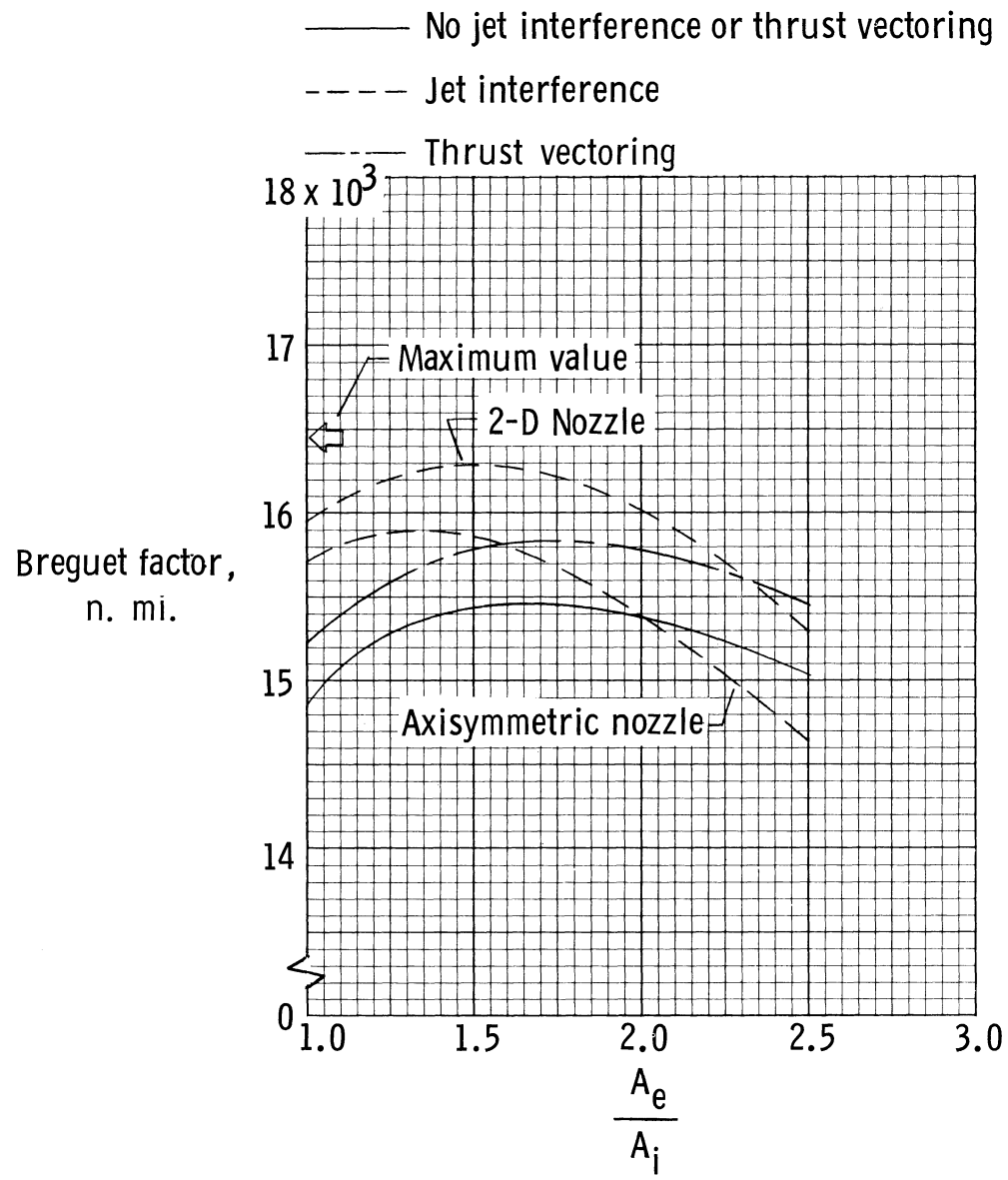

Figure 10.- Effect of jet interference and thrust vectoring on Breguet factor. Arrow indicates Breguet factor for optimum thrust vectoring and full expansion of nozzle flow without incurring drag penalty.

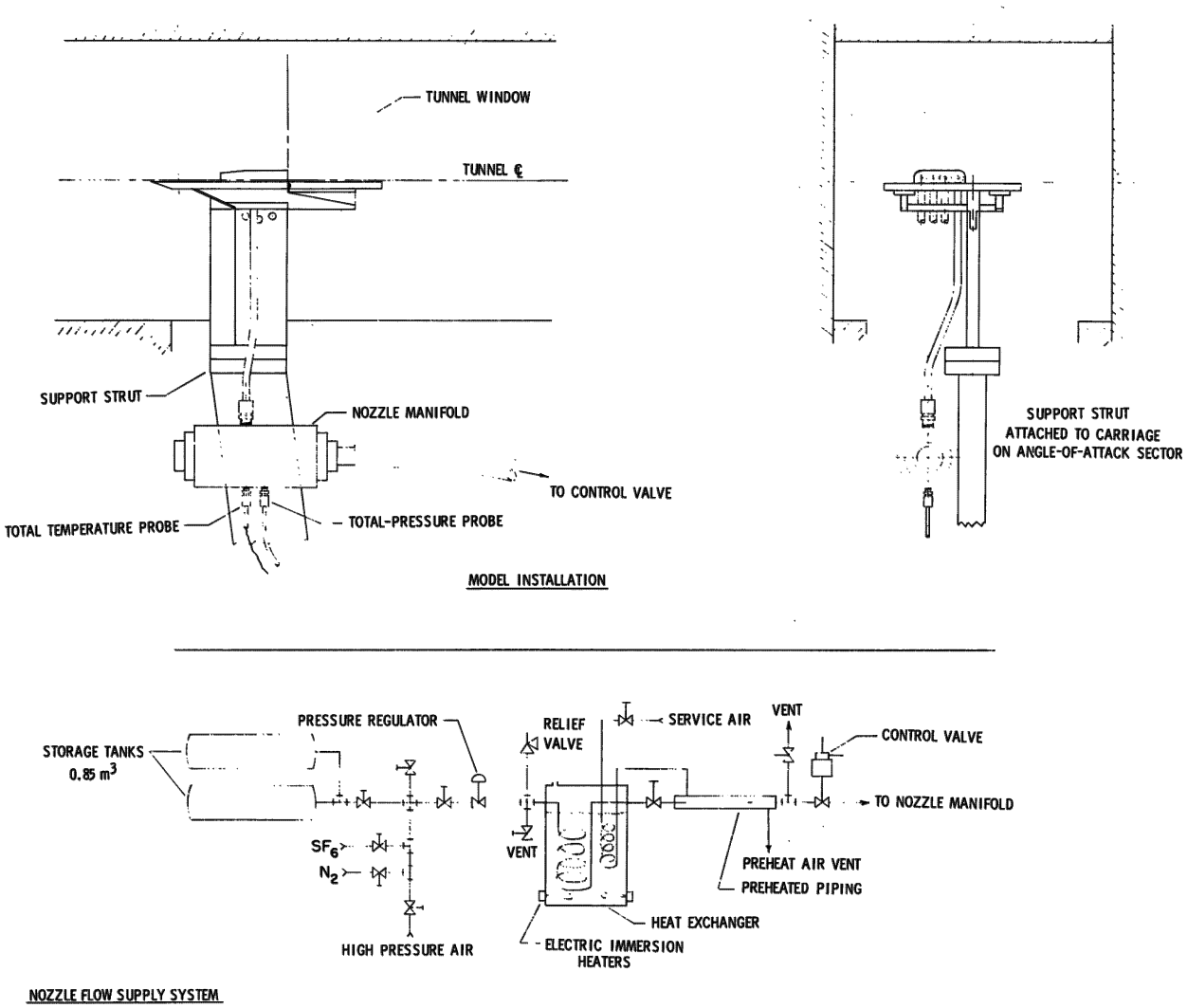

Figure 11.- Model installation and nozzle flow supply system.

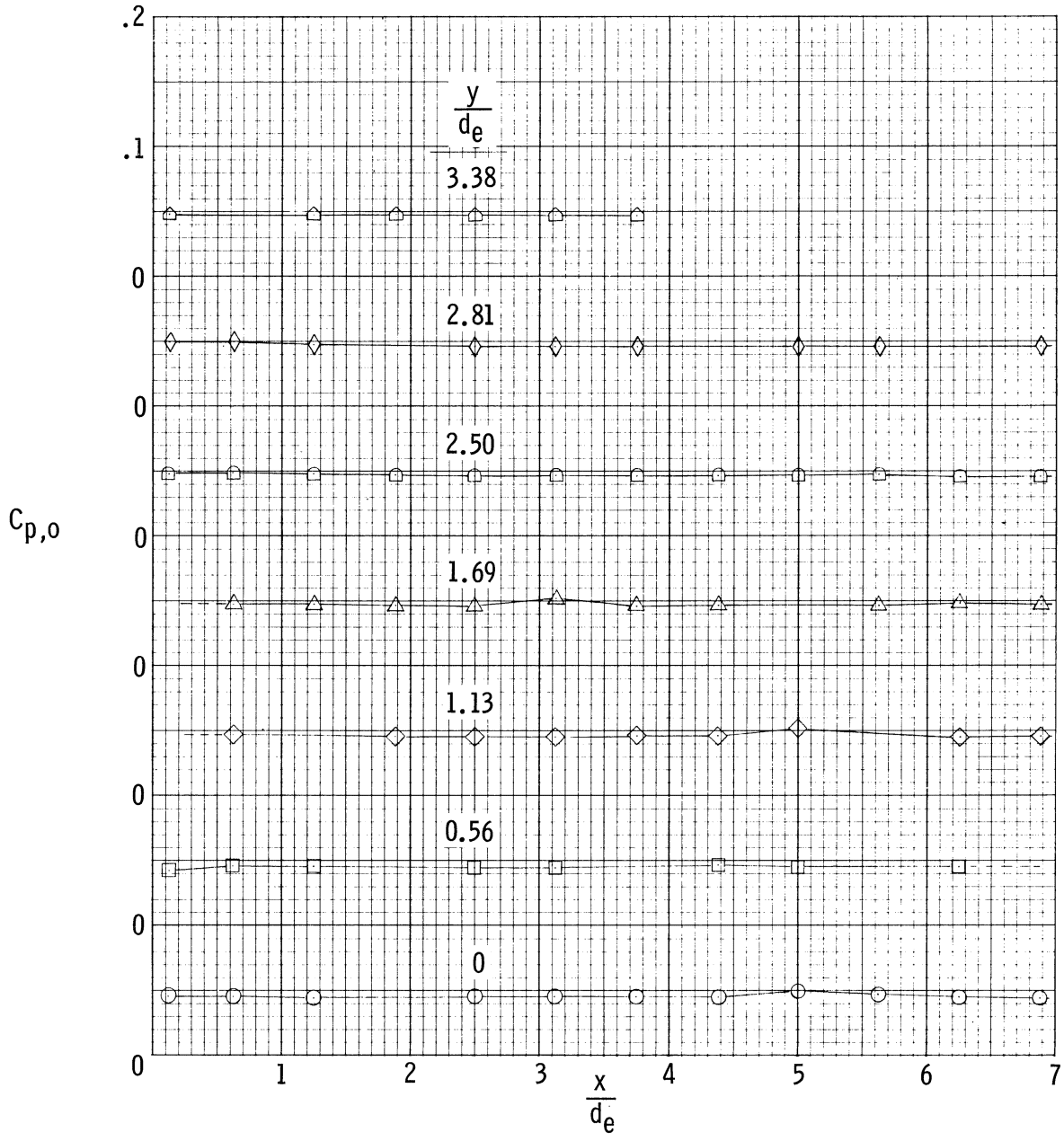

Figure 12.- Typical pressure coefficients on flat-plate model with engine off. $\alpha = 5^{o}$; $\epsilon = 0^{o}$.

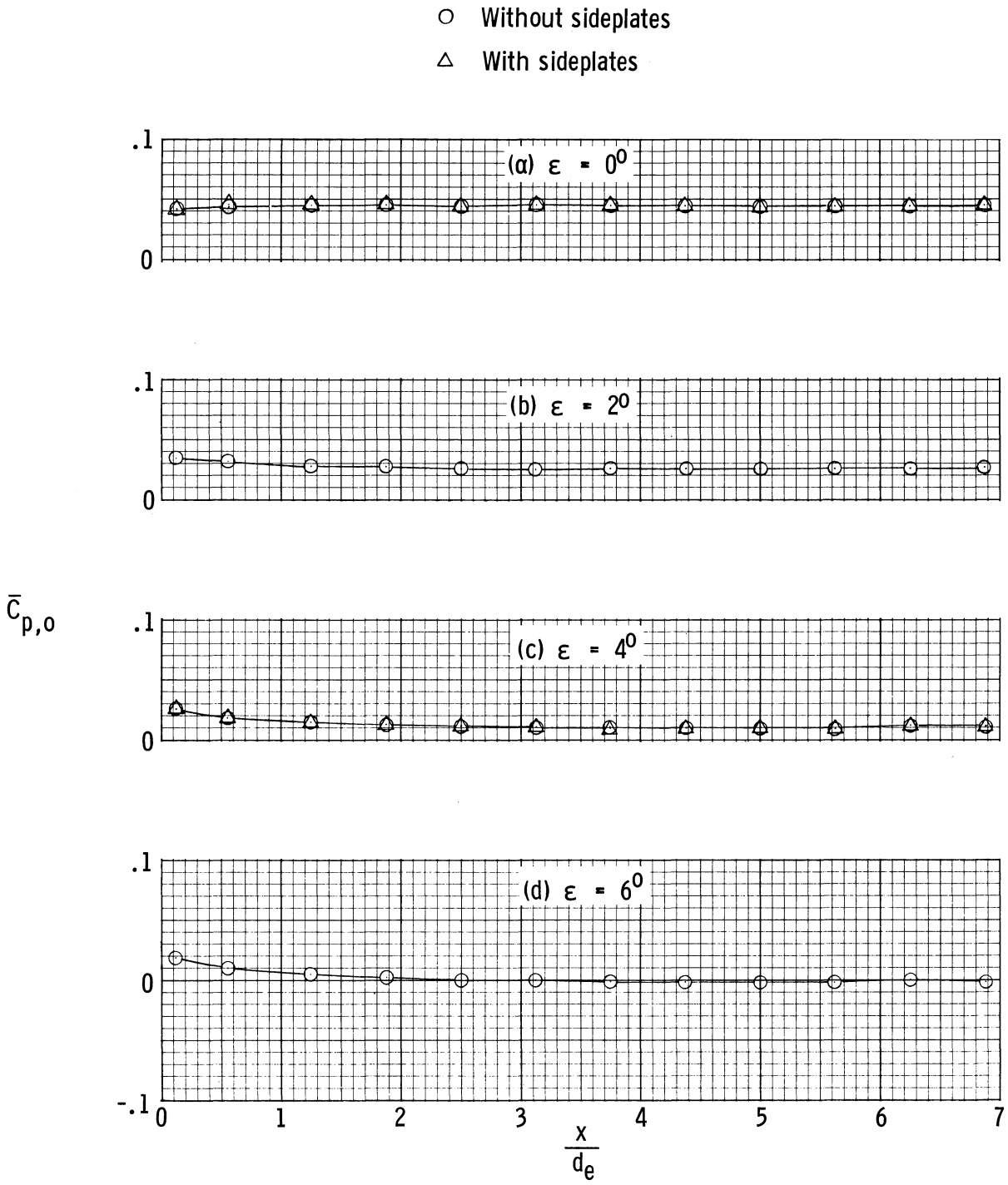

Figure 13.- Average spanwise pressure coefficients for flat-plate model with engine off. $\alpha = 5^{o}$.

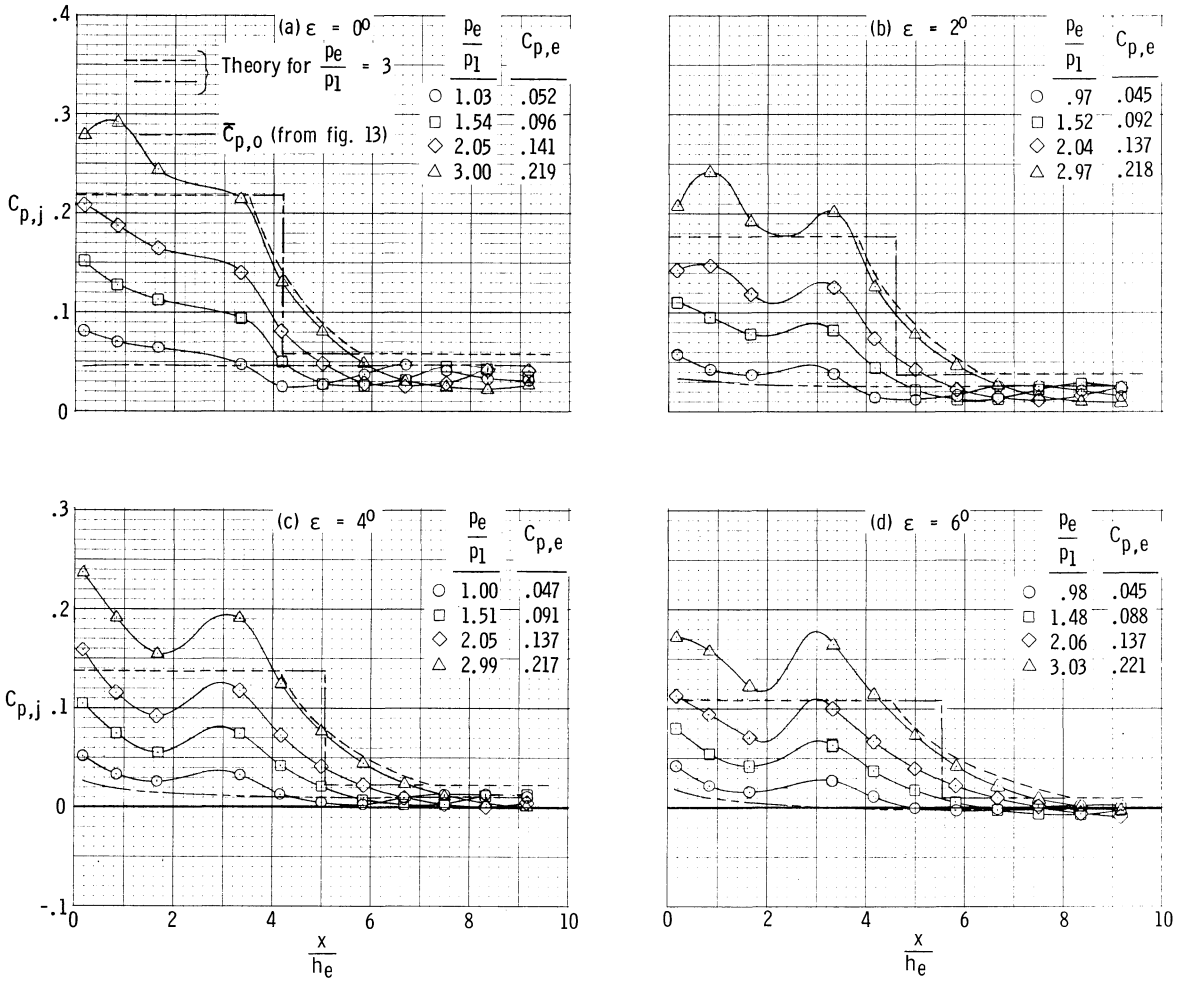

Figure 14.- Pressure distributions on flat-plate model downstream of nozzle exit along center line of 2-D nozzle. $\alpha = 5^{o}$.

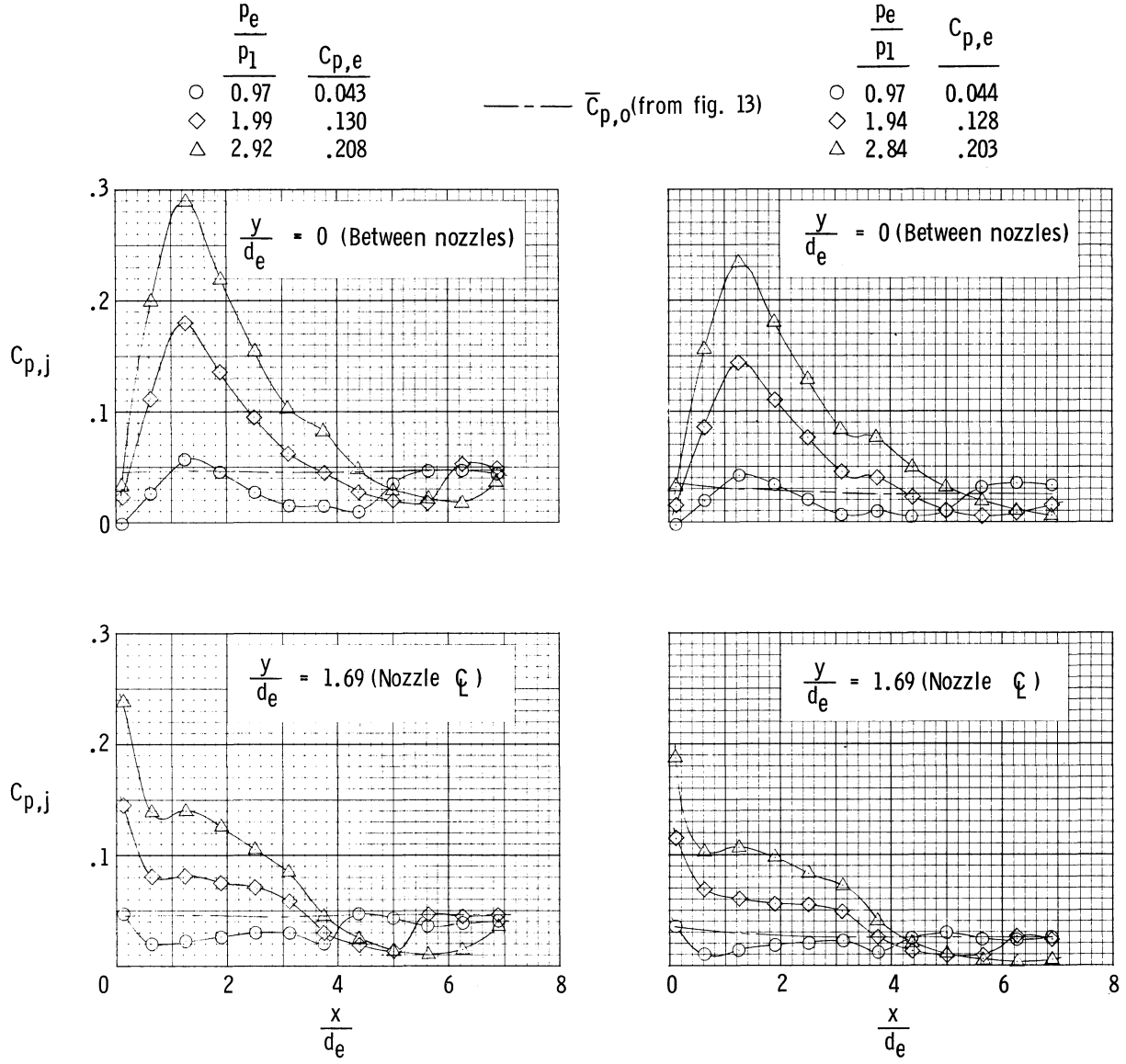

(a) $\epsilon = 0^o$.

(b) $\epsilon = 2^o$.

Figure 15.- Pressure-coefficient distributions on flat-plate model between adjacent nozzles and along nozzle center line downstream of axisymmetric nozzle exits. $\alpha = 5^o$; $\gamma_e = 1.4$.

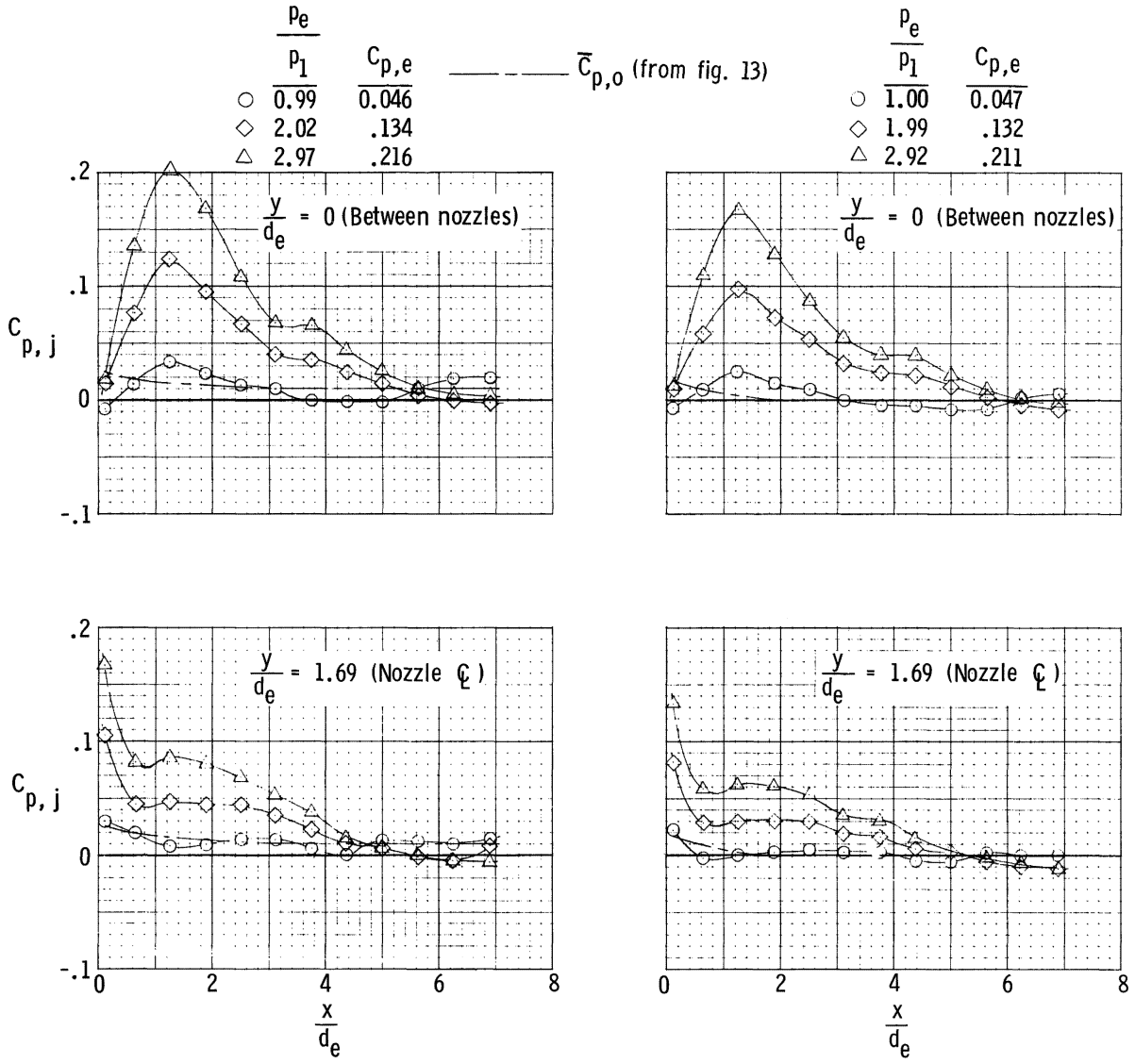

(c) $\epsilon = 4^{\circ}$.

(d) $\epsilon = 6^{\circ}$.

Figure 15.- Concluded.

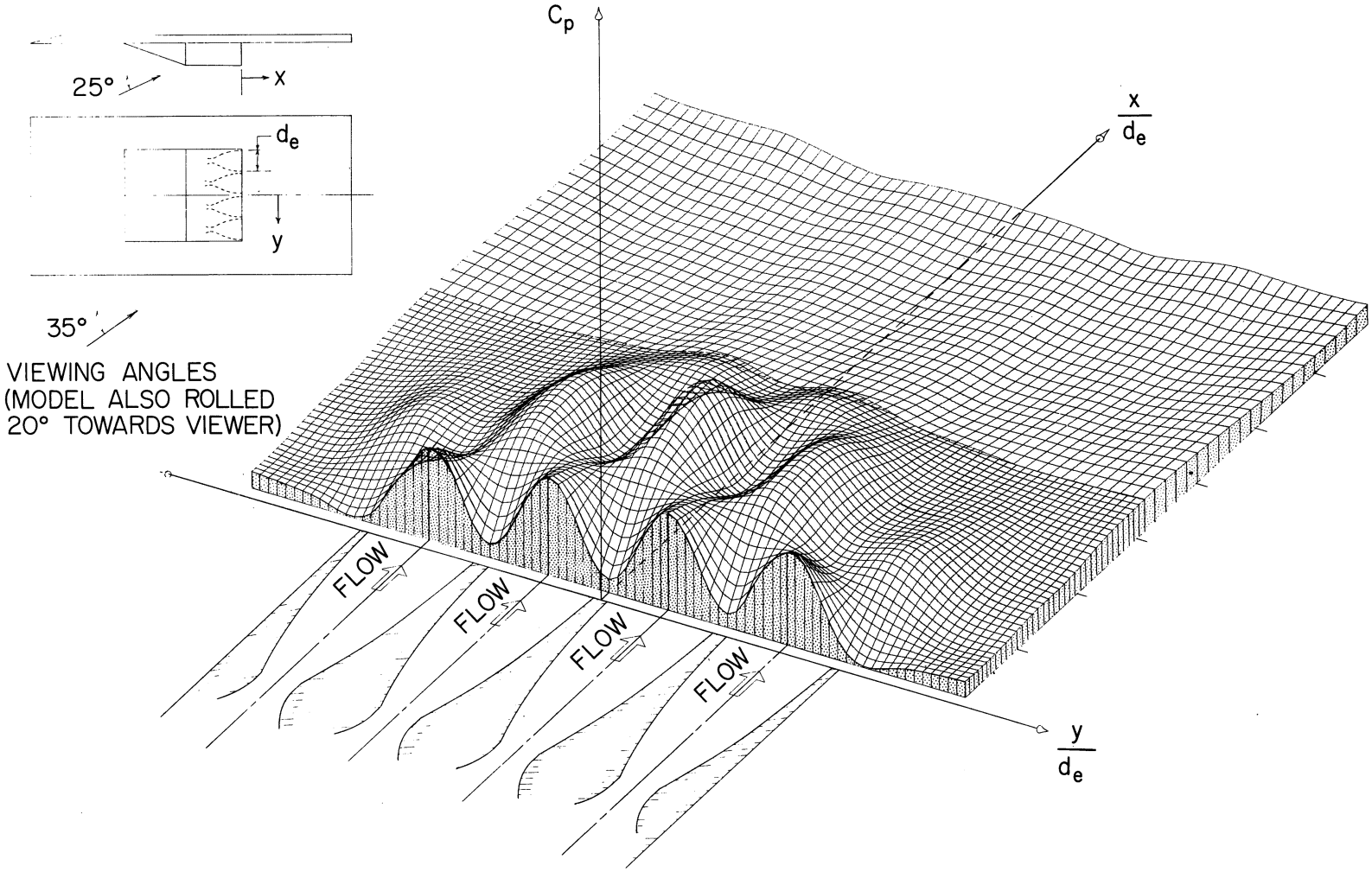

Figure 16.- Isometric view of pressure-coefficient distribution on flat-plate model with axisymmetric nozzles. $\alpha = 5^o$; $\epsilon = 0^o$; $p_e/p_1 = 2.92$.

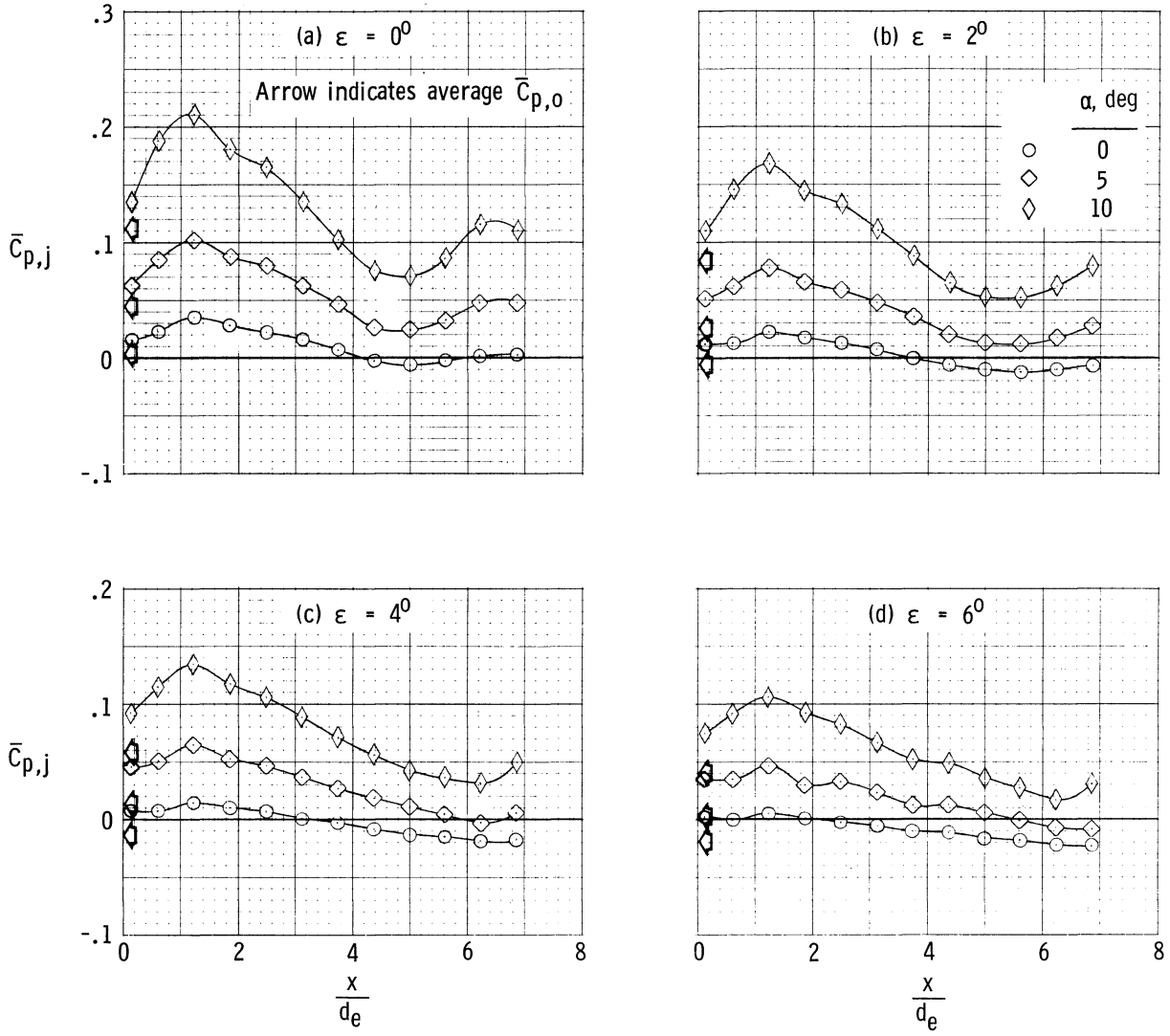

Figure 17.- Flat-plate model average pressure-coefficient distributions downstream of nozzle exits for three angles of attack. Axisymmetric nozzles with $p_e/p_1 \approx 2$.

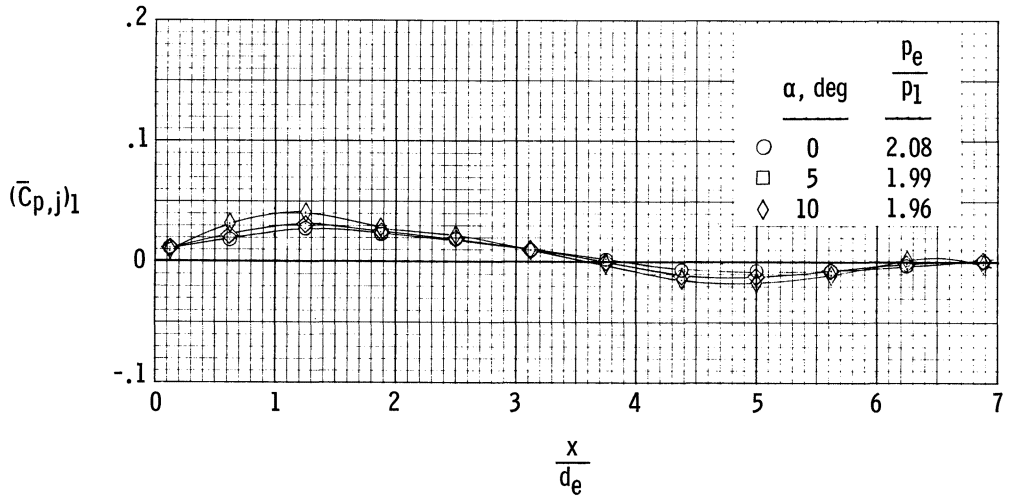

(a) $\epsilon = 0^o$.

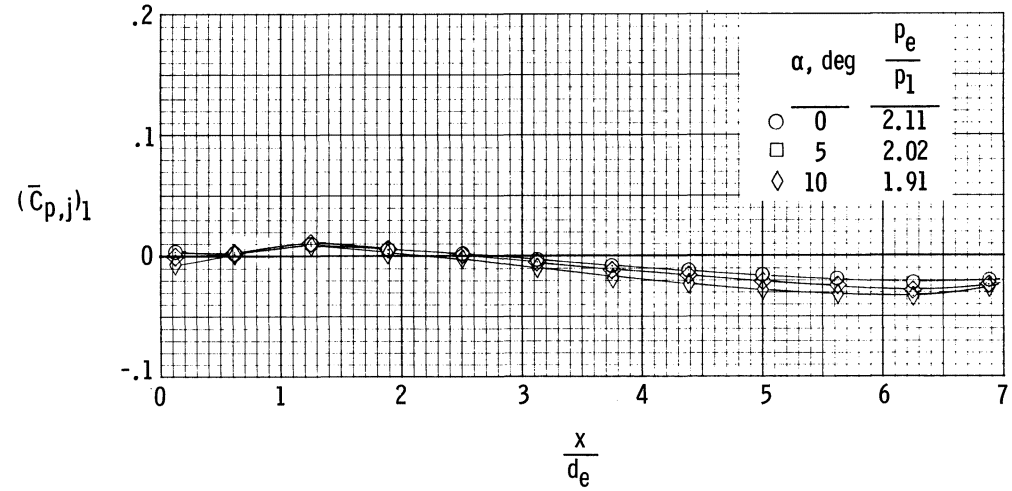

(b) $\epsilon = 4^o$.

Figure 18.- Comparison of jet-on pressure coefficients based on underwing conditions (p_1) of flat-plate model of three angles of attack. Axisymmetric nozzles; $\gamma_e = 1.4$.

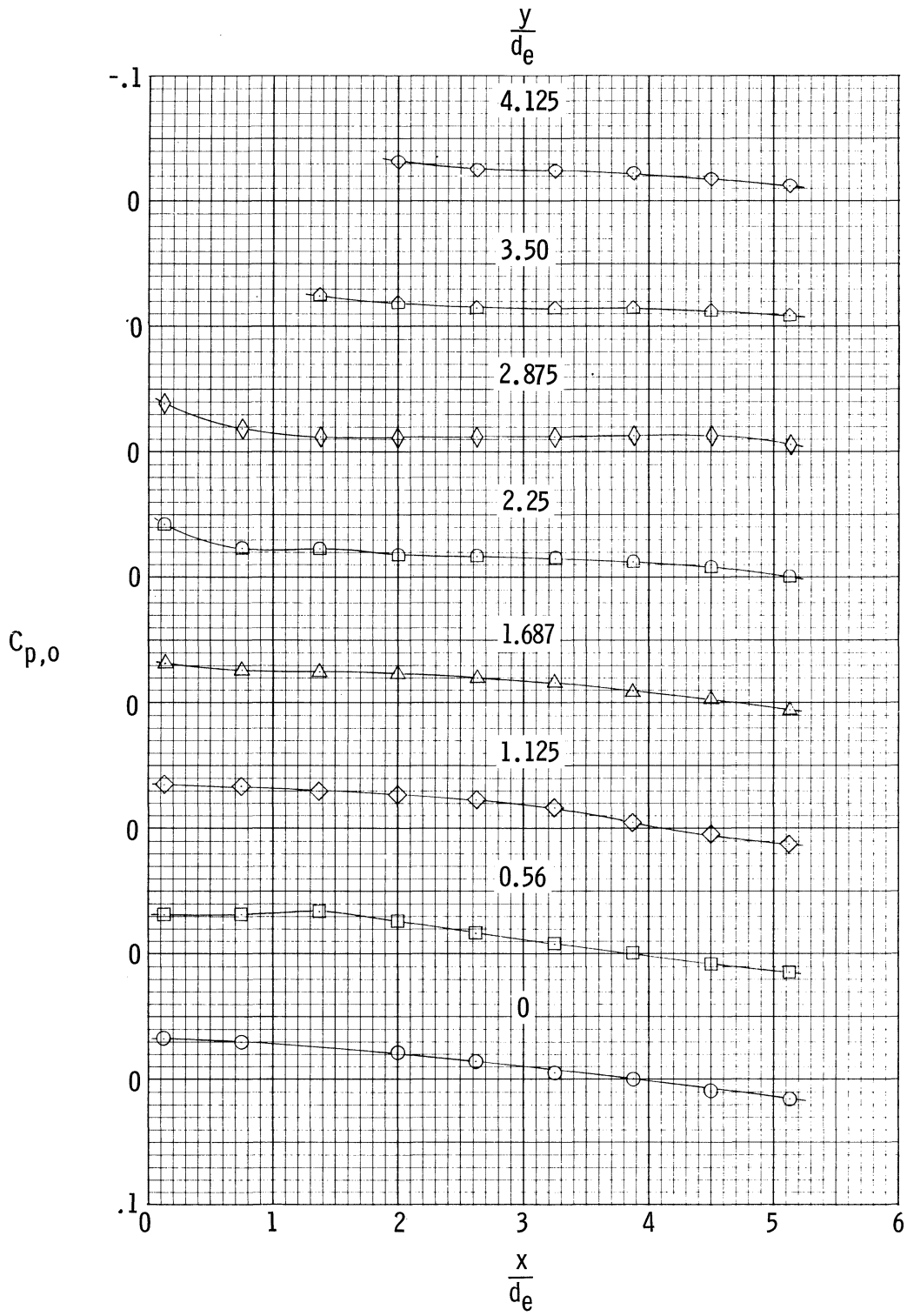

Figure 19.- Pressure coefficients on airplane model with engine off. $\alpha = 5^{o}$.

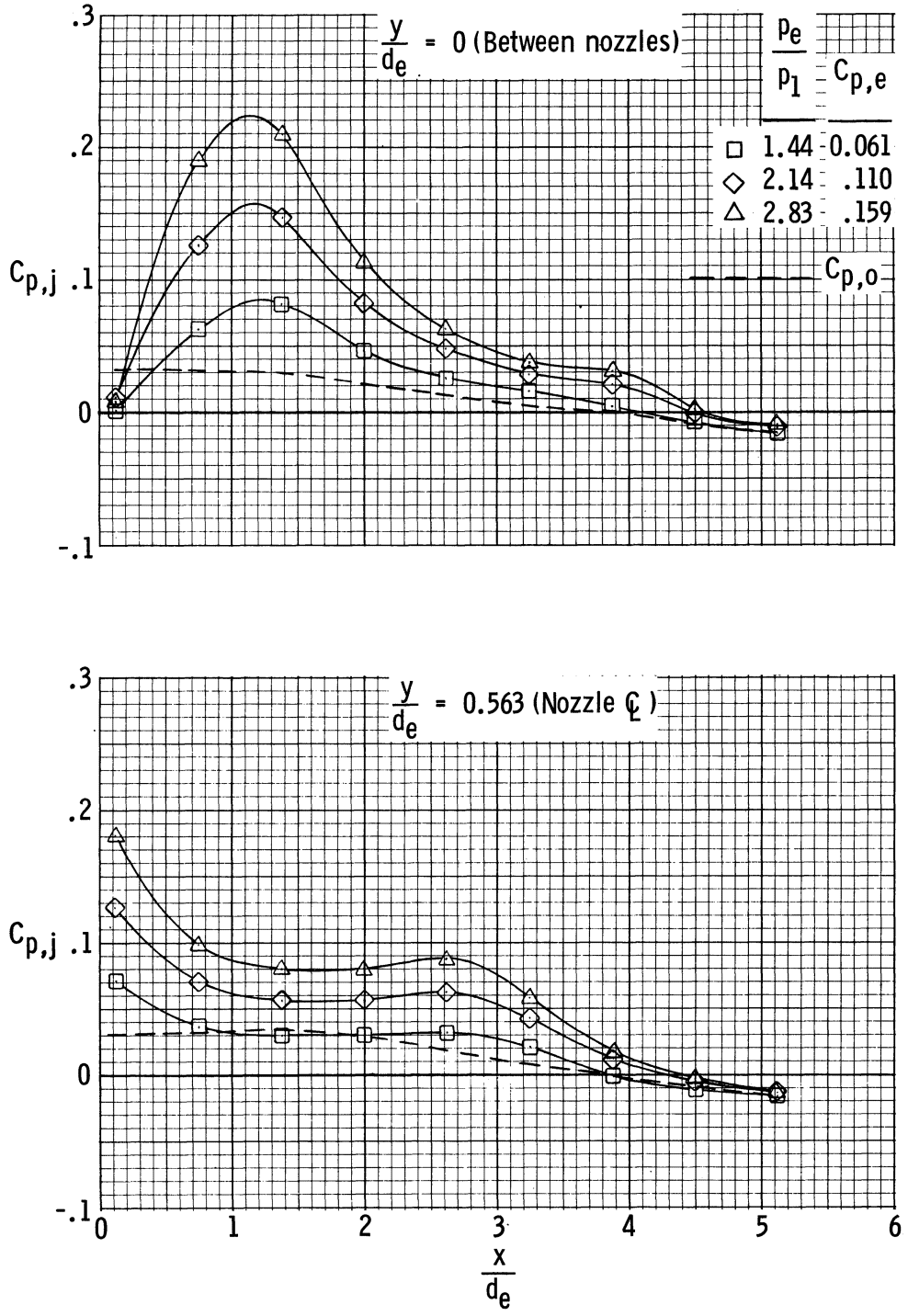

Figure 20.- Pressure coefficient distributions on airplane model between adjacent nozzles and along nozzle center line downstream of nozzle exits. $\alpha = 5^{o}$; $\gamma_e = 1.26$.

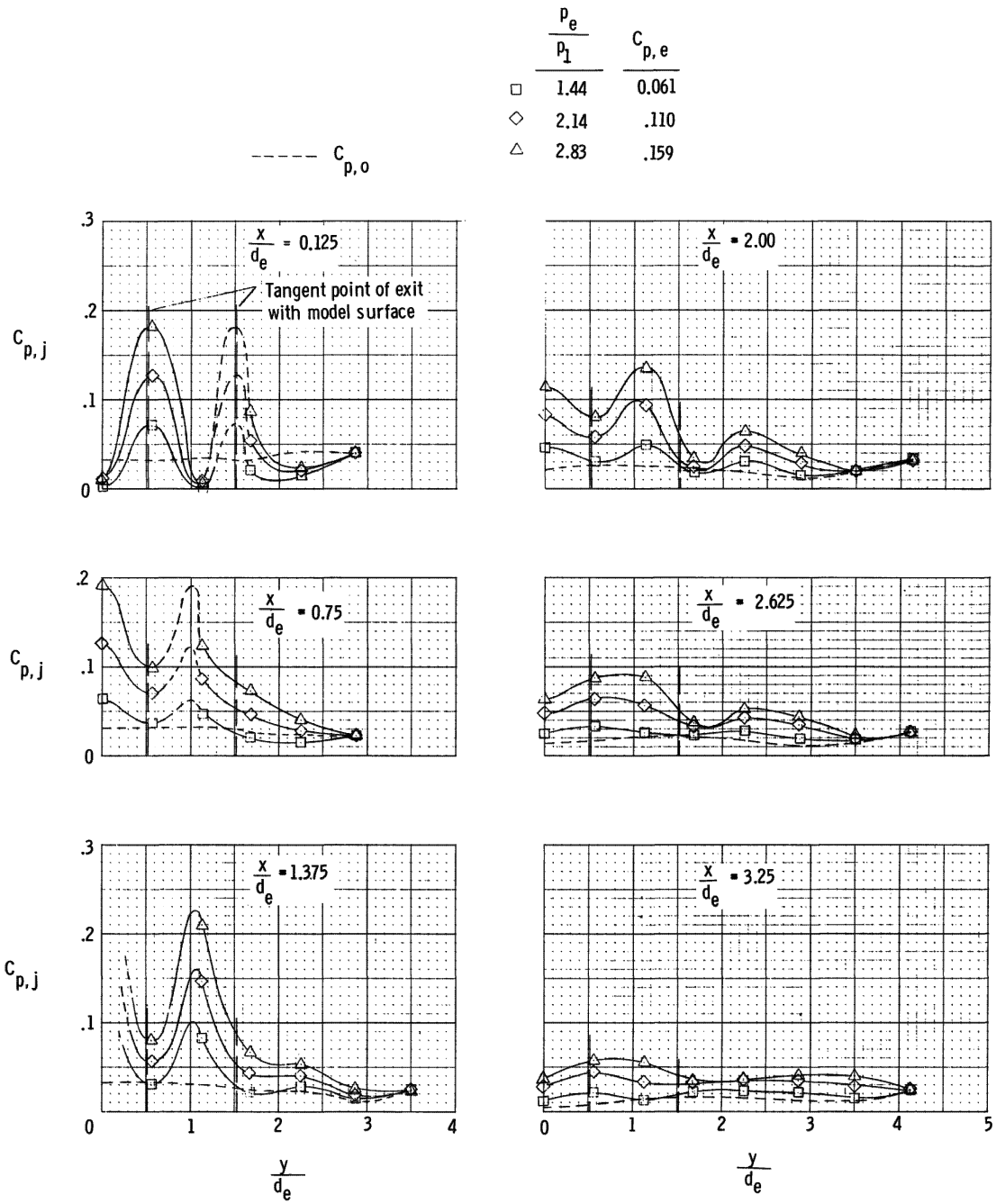

Figure 21.- Spanwise pressure-coefficient distributions on airplane model. $\alpha = 5^{o}$; $\gamma_e = 1.26$.

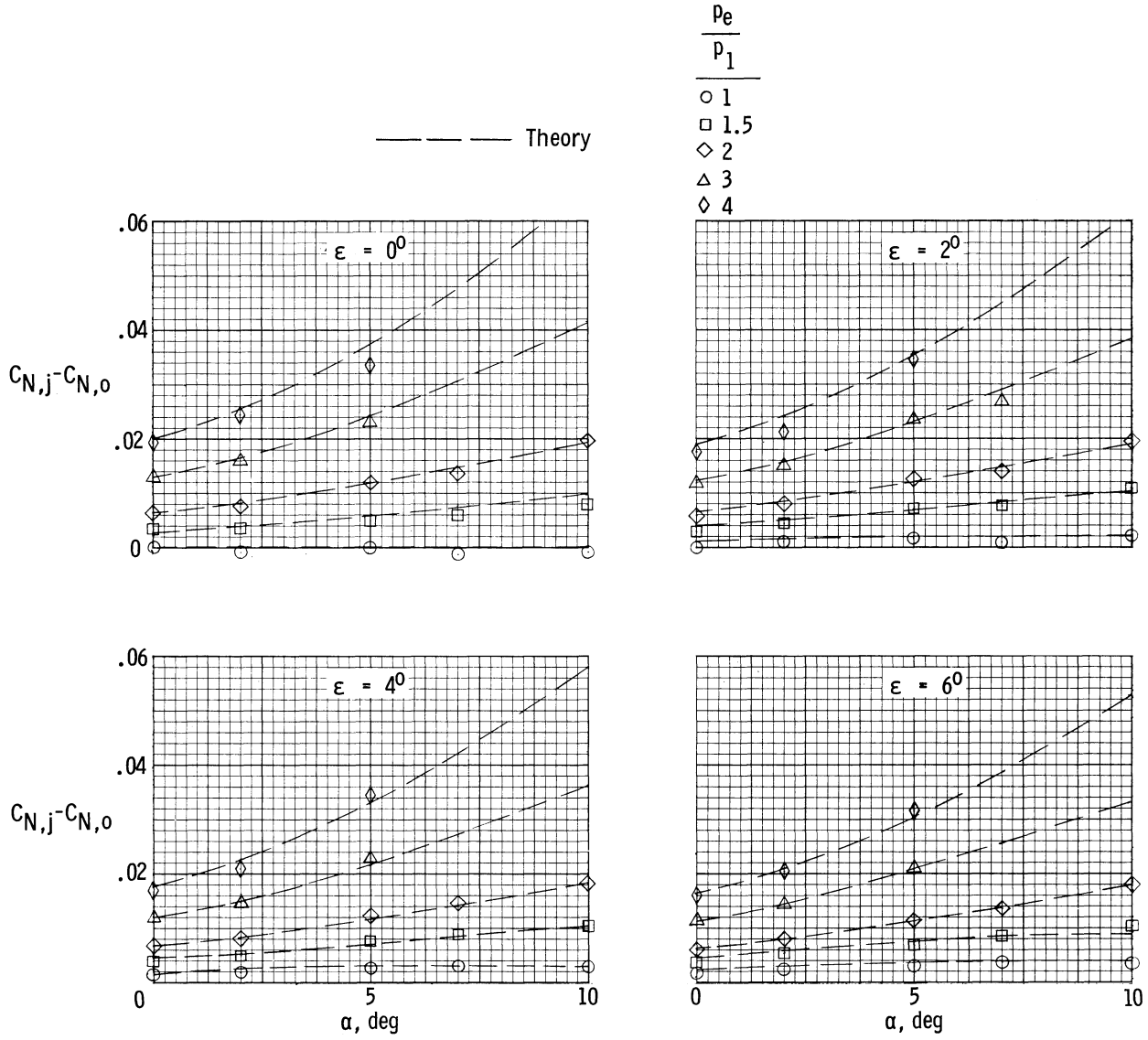

(a) 2-D nozzles.

Figure 22.- Variation of incremental normal-force coefficients due to jet flow with α for flat-plate model. A_{ref} = 452 cm^2; γ_e = 1.4; symbols used to identify faired values obtained from data.

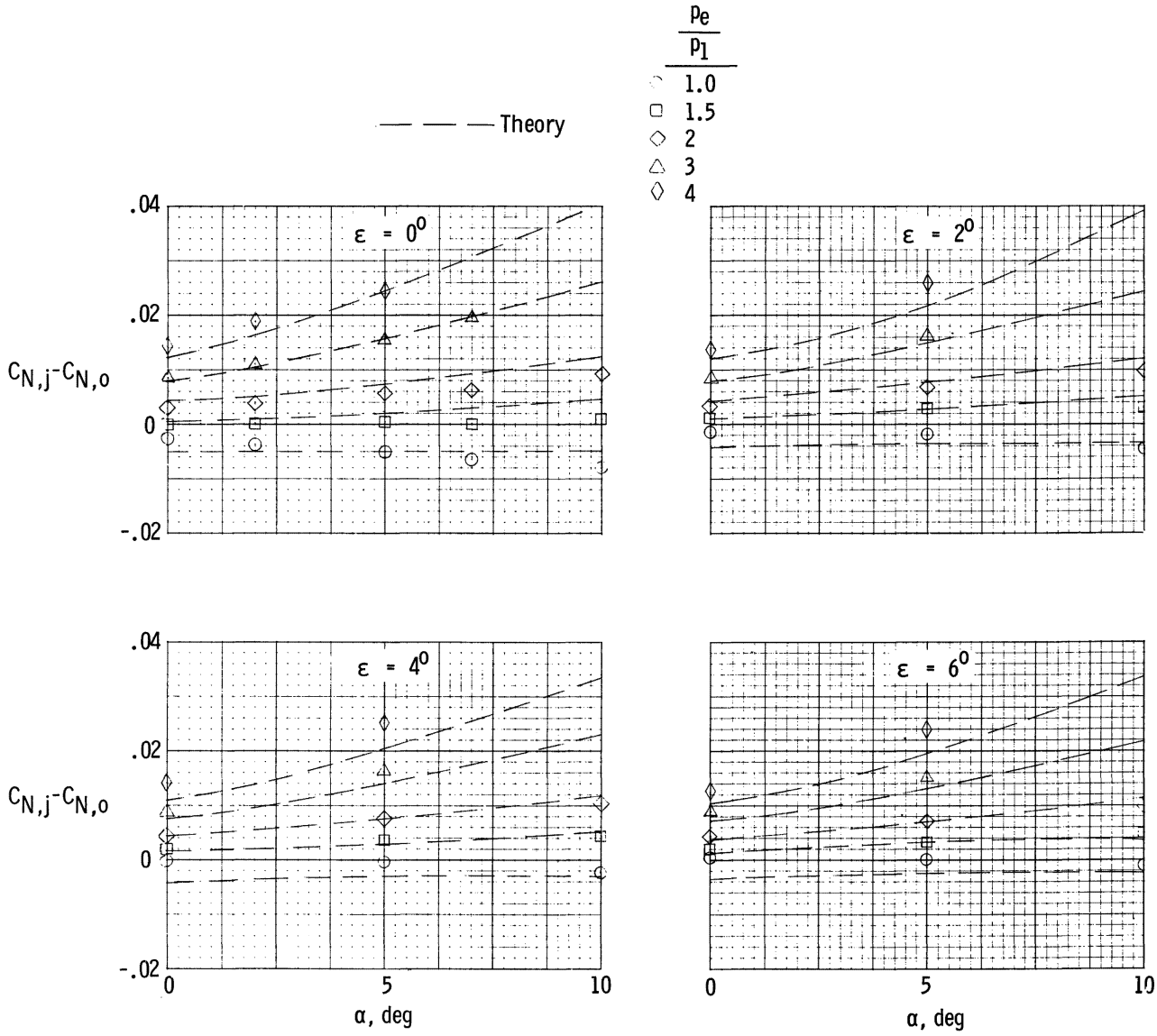

(b) Axisymmetric nozzles.

Figure 22.- Concluded.

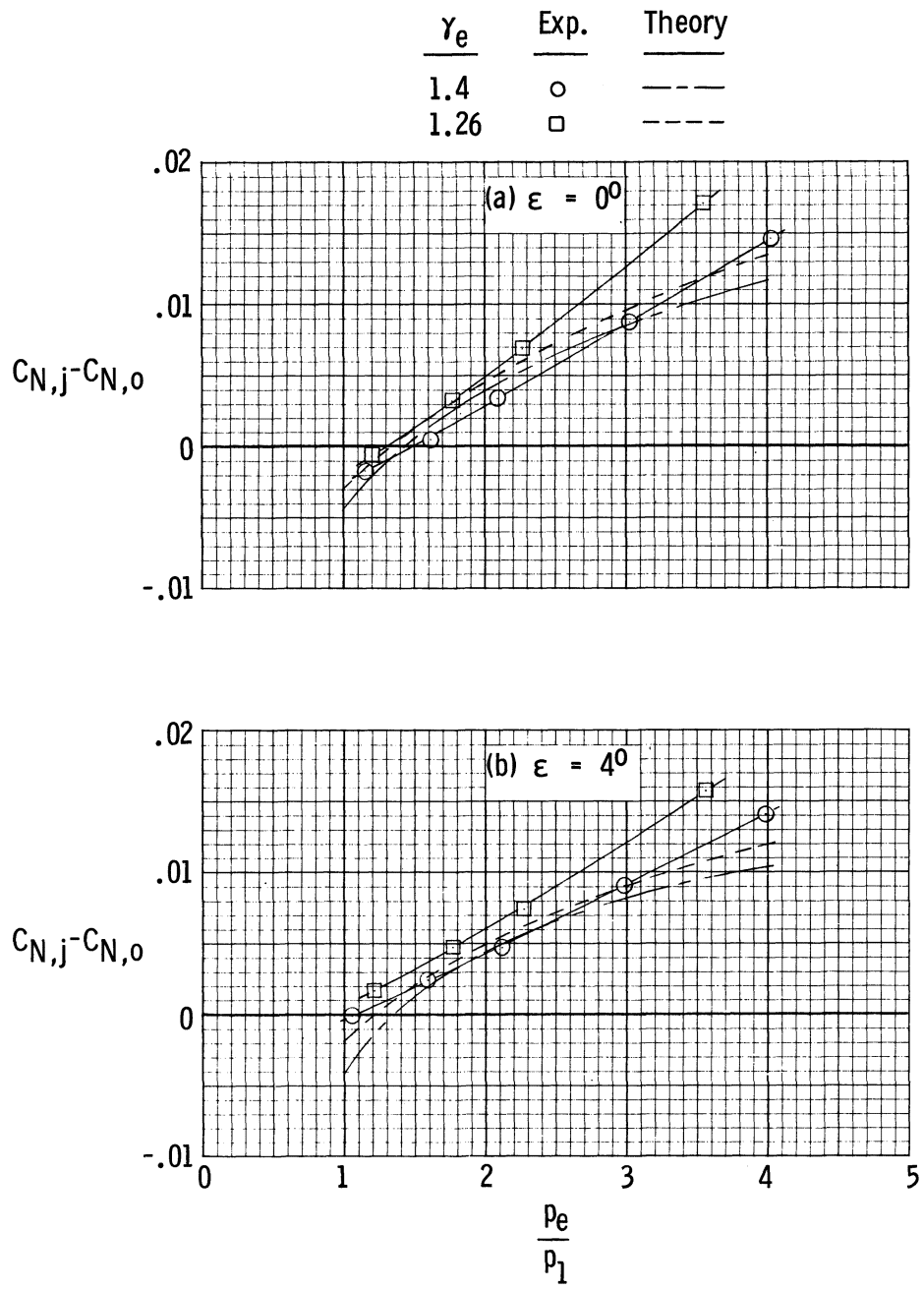

Figure 23.- Effect of γ_e on incremental normal-force coefficients. Flat-plate model at $\alpha = 0^o$; $A_{ref} = 452\ cm^2$.

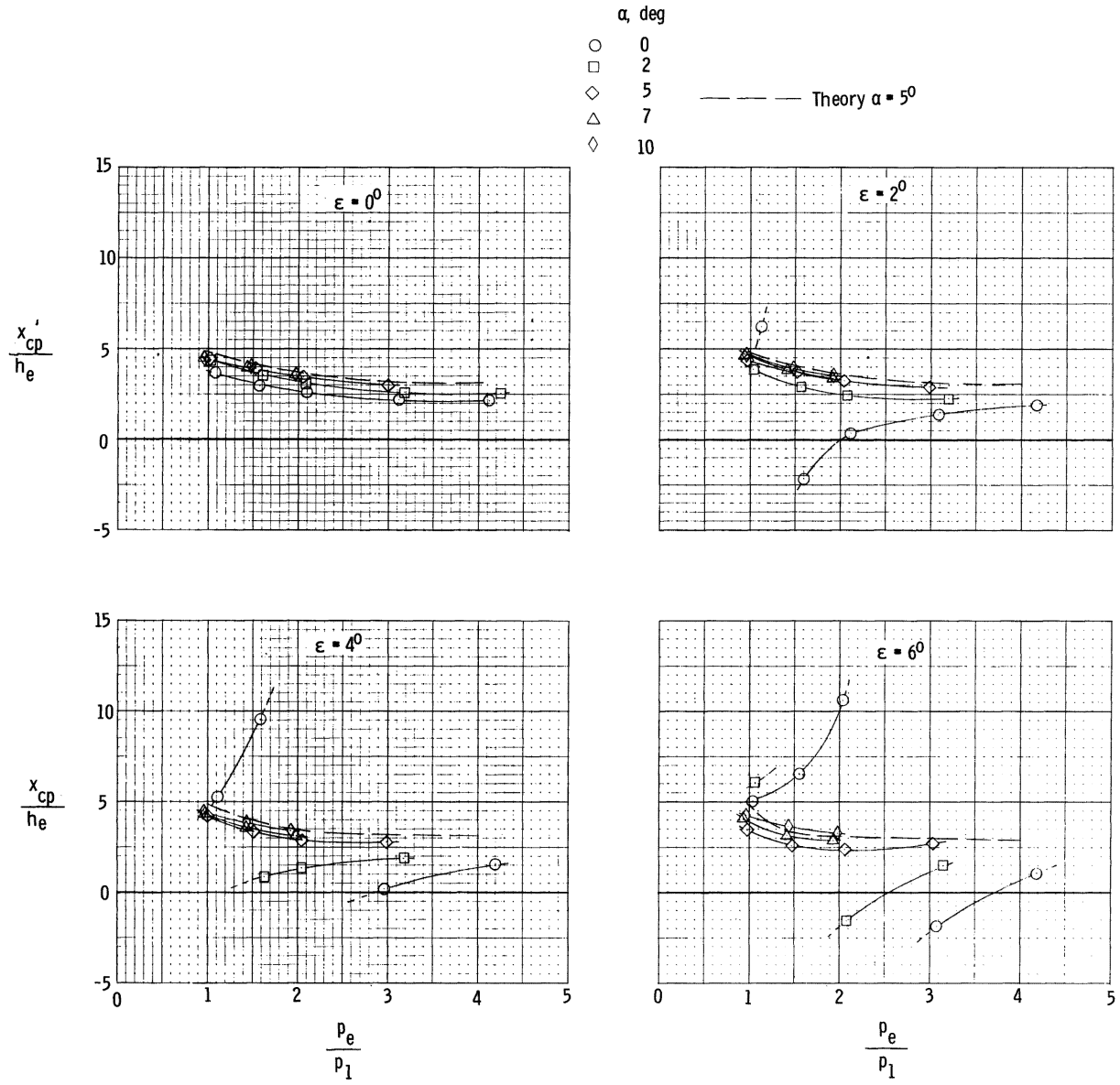

(a) 2-D nozzles.

Figure 24.- Variation of flap center-of-pressure location with nozzle pressure ratio for flat-plate model. l_{ref} = 43.2 cm; γ_e = 1.4.

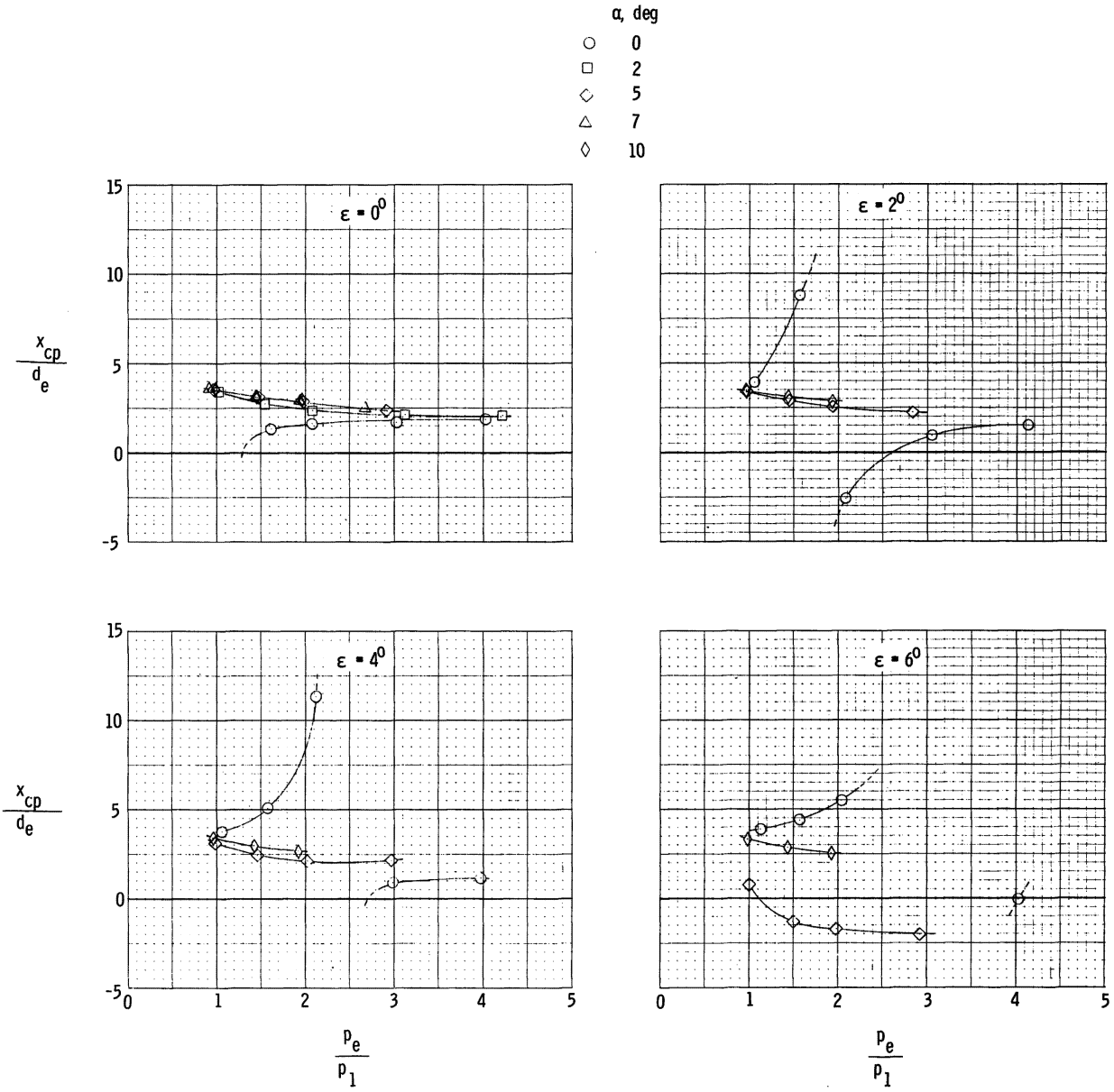

(b) Axisymmetric nozzles.

Figure 24.- Concluded.

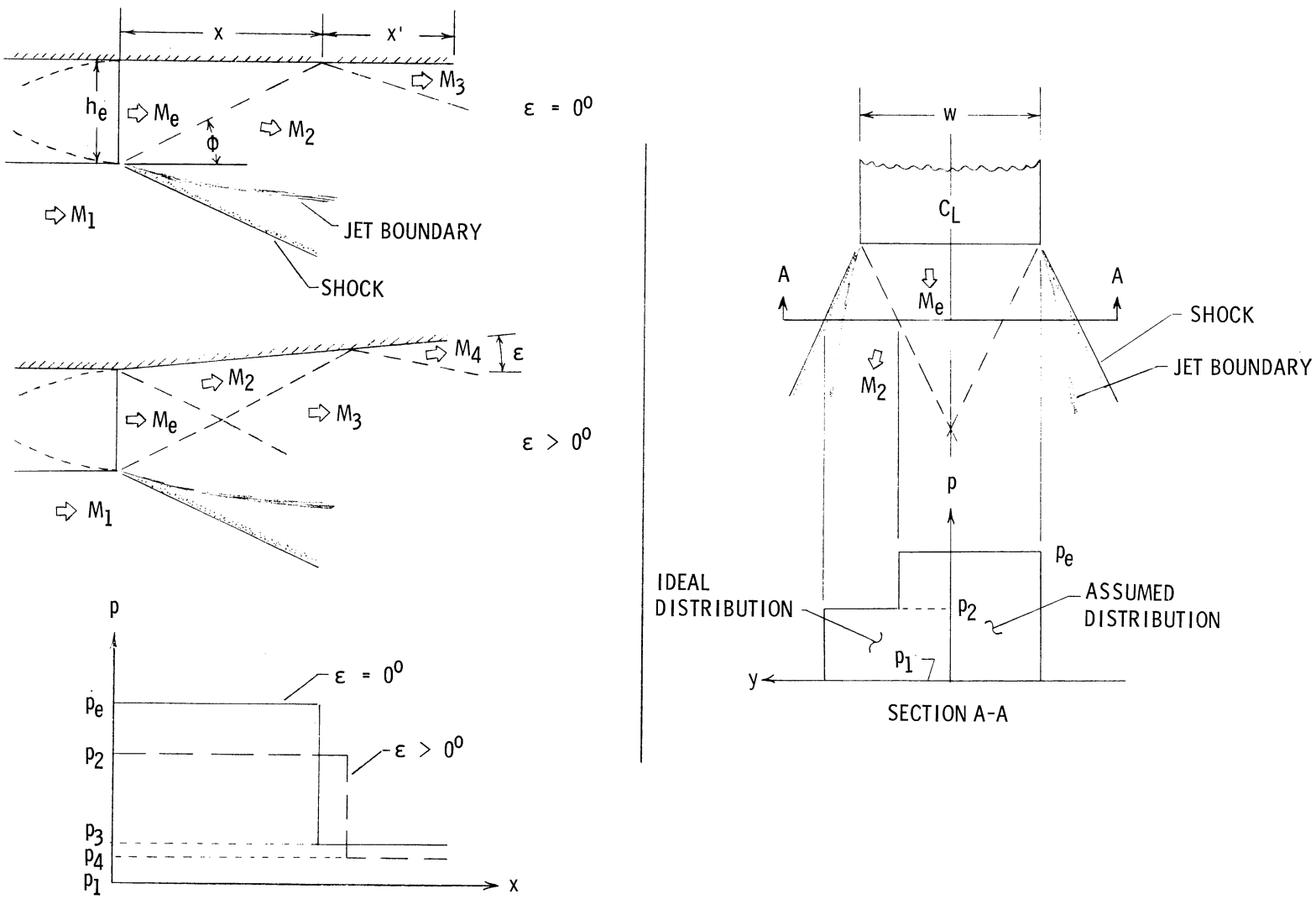

(a) Center-line pressure distribution.

(b) Spanwise pressure distribution.

Figure 25.- Flow model for calculation of forces on flat-plate model with 2-D nozzles.